

Electronic Thesis and Dissertation Repository

11-24-2014 12:00 AM

Investigation of Techniques to increase the Field of View of a Staring Transducer Array for Photoacoustic Imaging

Avery Raess, *The University of Western Ontario*

Supervisor: Dr. Jeffrey Carson, *The University of Western Ontario*

A thesis submitted in partial fulfillment of the requirements for the Master of Science degree in Medical Biophysics

© Avery Raess 2014

Follow this and additional works at: <https://ir.lib.uwo.ca/etd>

Recommended Citation

Raess, Avery, "Investigation of Techniques to increase the Field of View of a Staring Transducer Array for Photoacoustic Imaging" (2014). *Electronic Thesis and Dissertation Repository*. 2593.
<https://ir.lib.uwo.ca/etd/2593>

This Dissertation/Thesis is brought to you for free and open access by Scholarship@Western. It has been accepted for inclusion in Electronic Thesis and Dissertation Repository by an authorized administrator of Scholarship@Western. For more information, please contact wlsadmin@uwo.ca.

INVESTIGATION OF TECHNIQUES TO INCREASE THE FIELD OF VIEW OF A
STARING TRANSDUCER ARRAY FOR PHOTOACOUSTIC IMAGING

(Thesis format: Integrated Article)

by

Avery Raess

Graduate Program in Medical Biophysics

A thesis submitted in partial fulfillment
of the requirements for the degree of
Master of Science

The School of Graduate and Postdoctoral Studies
The University of Western Ontario
London, Ontario, Canada

© Avery Raess 2014

Abstract

Photoacoustic imaging (PAI) is a hybrid imaging modality that takes advantage of both optical and acoustic techniques for biomedical imaging. It is believed that PAI can successfully assess the margins of lumpectomy specimens in the operating room, decreasing the number of surgeries and wait time for patients. However, current PAI systems do not have sufficient field of view (FOV) to accommodate the size of lumpectomy specimens. In this work, transducer directionality and the use of a shaped matching layer were explored as means to increase the FOV of a staring photoacoustic transducer array. The results indicated that applying a convex matching layer to the face of transducers and directing them toward the centre of the array provides optimal sensitivity throughout the imaging volume. By employing these techniques, any PAI system's effective FOV can be increased without replacing existing transducers. The optimized system can now be investigated for lumpectomy margin assessment.

Keywords: Photoacoustic imaging, 3D imaging, field of view, staring transducer array, acoustic lens

Co-Authorship Statement

This section describes the contribution from other authors for the work in Chapters 2 and 3.

Chapter 2: A. Raess, P. Wong, I. Kosik, J.J.L. Carson. “Multi-Directional Staring Transducer Array for Photoacoustic Imaging”.

Mr. Wong wrote the code for calculation of signal fidelity measures and image reconstruction. Mr. Kosik aided in project conceptualization and built the transducers characterized for the array. Dr. Carson aided in project design, wrote code, edited the manuscript and provided project supervision. I wrote code, designed and conducted the experiments, analysed and interpreted results, and wrote the manuscript.

Chapter 3: A. Raess, M. Van De Kleut, I. Kosik, P. Wong, J.J.L. Carson.

“Implementation of a shaped matching layer as an acoustic lens for transducers in a staring transducer array for photoacoustic imaging”.

Ms. Van De Kleut performed the physical experiments including application of the matching layer and transducer characterization. Mr. Kosik built the transducers and assisted with matching layer application and research design. Mr. Wong wrote the code for the calculation of signal fidelity measures and image reconstruction. Dr. Carson aided in project design, wrote code, edited the manuscript and provided project supervision. I supervised physical experiments, wrote the simulation code, performed simulated experiments, analysed and interpreted results and wrote the manuscript.

Acknowledgments

This work would not have been possible without the help and support of the following individuals.

Dr. Carson, I could never thank you enough for the support you have given me over the last two years. Your motivation, inspiration, and all of the work you have put into the lab are truly appreciated. Thank you for the tough love and pushing me when I needed it the most. Your work ethic and commitment to the lab make you not only a great mentor but an amazing role model as well.

To all of the members of the Carson lab: Astrid, Phil, Ivan, Pantea, Madeleine, Esther, Mohamadreza, and Morteza. I would like to thank every one of you for your time and contribution to both my scientific and personal growth. It has been a pleasure working with you and I couldn't have asked for a better group of people to spend my time with.

I would like to thank all the friends and family that have supported me throughout my education thus far. Thank you for caring about me enough to feign interest when I start talking about Matlab errors for the thousandth time, and for the reassuring and motivational words regarding whatever I happen to be disproportionately freaking out about at that moment. Thank you for your patience, your presence, and your love.

Finally, I would like to acknowledge financial support from the Western Graduate Research Scholarship (WGRS), the Ontario Graduate Scholarship (OGS), the Translational Breast Cancer Research Unit (TBCRU) and the Breast Cancer Society of Canada (BCSC), the Strategic Training Program in Cancer Research and Technology Transfer (CaRTT), and the Canadian Institutes of Health Research (CIHR).

Table of Contents

Abstract.....	ii
Co-Authorship Statement.....	iii
Acknowledgments.....	iv
Table of Contents.....	v
List of Figures.....	ix
List of Abbreviations and Symbols.....	xii
Preface.....	xiii
Chapter 1.....	1
1 Introduction.....	1
1.1 Background.....	1
1.2 Applications.....	1
1.3 Photoacoustic imaging theory.....	3
1.3.1 Photoacoustic wave generation.....	3
1.3.2 Photoacoustic wave propagation.....	4
1.4 Imaging methods.....	5
1.5 System design.....	7
1.5.1 Transducers for photoacoustic wave detection.....	7
1.5.2 Transducer arrangement and scanning patterns.....	9
1.5.3 Transducer-dependent system properties.....	11
1.6 Advanced methods for assessing system performance.....	13
1.6.1 Crosstalk matrix.....	13
1.6.2 Signal fidelity measures.....	14
1.7 Motivation and Objectives.....	15
1.7.1 Lumpectomy margin assessment in the operating room.....	15

1.7.2 Objectives	17
1.7.3 Approach	18
1.8 References	19
Chapter 2	26
2 Multi-directional staring array for photoacoustic imaging	26
2.1 Introduction	26
2.1.1 Background.....	26
2.1.2 Photoacoustic transducer arrays	26
2.1.3 Objective and Approach	27
2.2 Methods	27
2.2.1 Characterization of System Components	27
2.2.2 Simulated Model of Photoacoustic Imaging System.....	30
2.2.3 Image reconstruction	31
2.2.4 Imaging Experiment	31
2.2.5 Evaluation methods	32
2.2.6 Performance Metrics.....	32
2.3 Results	32
2.3.1 Crosstalk matrix.....	32
2.3.2 Imaging task	36
2.4 Discussion	40
2.4.1 Crosstalk matrix.....	40
2.4.2 Imaging task	41
2.4.3 Implementation and Considerations	42
2.5 Conclusion.....	43
2.6 References	44

Chapter 3.....	47
3 Implementation of a shaped matching layer as an acoustic lens for transducers in a staring transducer array for photoacoustic imaging.....	47
3.1 Introduction.....	47
3.1.1 Background.....	47
3.1.2 Photoacoustic transducer limitations.....	47
3.1.3 Acoustic lens material.....	48
3.1.4 Objective and Approach.....	48
3.2 Methods.....	49
3.2.1 Transducer matching layer and characterization.....	49
3.2.2 Modelling of Photoacoustic Imaging System.....	52
3.2.3 Evaluation methods.....	52
3.3 Results.....	53
3.3.1 Transducer array simulated response.....	53
3.4 Discussion.....	57
3.4.1 Transducer and matching layer characterization.....	57
3.4.2 Simulated photoacoustic imaging system.....	58
3.5 Conclusion.....	59
3.6 References.....	60
Chapter 4.....	62
4 Discussion and Future Work.....	62
4.1 System characterization.....	62
4.1.1 Photoacoustic point source.....	62
4.1.2 Transducer characterization.....	64
4.1.3 System characterization.....	67

4.2 Increasing the field of view of a photoacoustic transducer array.....	68
4.3 Image reconstruction.....	69
4.4 System analysis.....	70
4.5 Applications.....	70
4.5.1 A photoacoustic imaging system for lumpectomy margin assessment.....	70
4.6 Summary and conclusions.....	72
4.7 References.....	73
Curriculum Vitae.....	75

List of Figures

Figure 1.1: Absorption coefficient spectra of tissue chromophores, adapted from Beard et al. [7]. Water, solid black line; oxyhaemoglobin, red line; deoxyhaemoglobin, blue line; melanin, black dashed line; lipid, brown line. 2

Figure 1.2: Pressure profile of a theoretical photoacoustic wave in the time domain. 5

Figure 1.3: Photograph of the photoacoustic imaging system, with the laser source, optical illumination fibers (black fibers), transducer array, data acquisition (DAQ) system and personal computer (PC) indicated with labels. 7

Figure 1.4: Transducer orientations. (a) A single transducer showing a raster scanning movement, (b) a linear array of transducers, (c) an arc array of transducers and (d) a spherical array of transducers showing a rotational movement. 11

Figure 1.5: Representation of the field of view of a spherical transducer array. Three transducers are shown with their respective field of views contributing to the field of view of the array (green sphere). 13

Figure 2.1: (a) Characterization of the photoacoustic point source along the azimuthal and (b) zenith directions. Each point is the mean of three trials with one standard deviation shown as error bars. (c) Pressure wave amplitude was measured as a function of distance from the transducer face, where each point is an average of three trials and one standard deviation above and below the mean is shown with error bars. An equation fitted to the data is shown as a blue line. (d) Normalized photoacoustic signal intensity shown as a function of the angle away from normal to the transducer face in degrees. Each point is independent and an equation fitted to the data is shown in blue. 29

Figure 2.2: (a) Representative photoacoustic signal used for modeling system response. (b) Relative sensitivity of the representative transducer away from normal. (c) Point cloud representation of the 129 transducer locations in the stationary array. (d) Point cloud representation of 8, 27, 64 and 125 directional point locations, from left to right, top to bottom respectively, at 14 mm cube spacing. 31

Figure 2.3: Intensity maps indicating the (left to right) sensitivity, aliasing of the centre voxel and aliasing of an edge voxel of the photoacoustic imaging system due to variation of transducer directions within the array. The xy, xz and yz planes through the centre of the volume are shown in the top, middle and bottom of each set of three intensity maps, respectively. The spacing of the directional points in the array was 0 to 14 mm, from left to right along each row of intensity maps. The number of directional points increases from 8 to 125 from the top to bottom for each grouping of three intensity maps. 33

Figure 2.4: Mean absolute error and structural similarity index are shown in the left and right columns, respectively. The number of directional points increases from the top to bottom graph and the spacing of the directional points is indicated in the legend in the top left graph, from 0 mm to 14 mm. The concentric hollow cube index indicates a 1 mm

thick cube within the imaging volume from the outside (index 1) to inside (index 10) of the volume.....	34
Figure 2.5: Mean absolute error and structural similarity index are shown in the left and right columns, respectively, as intensity maps. The xy, xz and yz planes through the centre of the volume are shown in the top, middle and bottom of each set of three intensity maps, respectively. The spacing of the directional points in the array was 0 to 14 mm, from left to right along each row of intensity maps. The number of directional points increases from 8 to 125 from the top to bottom for each grouping of three intensity maps.	36
Figure 2.6: (a) The xy, xz and yz planes through the centre of the imaging phantoms. The scale bar applies to all images. (b) Reconstructed images utilizing increasing spacing of directional points (left to right) and number of directional points (top to bottom) within the transducer array are shown for the array of point sources (centre) and Shepp-Logan phantom (right).	38
Figure 2.7: Mean absolute error (top) and structural similarity index (bottom) for the phantom imaging tasks are shown for the array of point sources (left) and Shepp-Logan phantoms (right).....	39
Figure 3.1: The cross-section of a 3D representation of the transducer face, where (a) has no matching layer, (b) has a flat epoxy matching layer and (c) has a convex epoxy matching layer. The scale bar represents 1 mm in all cases and the transducer element is approximately 5 mm in diameter.	50
Figure 3.2: Normalized signal amplitude of the transducers as a function of angle away from normal to the transducer face with (a) no matching layer, (b) a flat matching layer and (c) a convex matching layer. The empirically determined equations fit to (a), (b) and (c) are shown in (d). (d) Fitted equations to transducer response with no matching layer (blue line), a flat matching layer (red line) and a convex matching layer (black line).	51
Figure 3.3: Parameters of the simulated photoacoustic imaging system. (a) A point cloud representation of the location of transducers within a hemispherical staring array with a radius of 48 mm. (b) Representative signal attained from averaging 64000 signals from a point-like source.....	52
Figure 3.4: Intensity maps indicating the (left to right) sensitivity, aliasing of the centre voxel and aliasing of an edge voxel of the photoacoustic imaging system for three matching layer cases (top to bottom): no matching layer, a flat epoxy matching layer and a convex epoxy matching layer. Sensitivity maps are shown from 0 to 80% of the maximum sensitivity and aliasing maps are normalized to 1, corresponding to the signal amplitude in the respective voxel. The 25 mm x 25 mm xy, xz and yz planes through the centre of the volume are shown in the top, middle and bottom of each set of three intensity maps, respectively.	54

Figure 3.5: Mean absolute error and structural similarity index are shown in the left and right panels, respectively. No matching layer, a flat matching layer and convex matching layer are shown in blue, red and black, respectively. The concentric hollow cube index indicates a 1 mm thick cube within the imaging volume from the outside (concentric hollow cube index 1) to inside (index 10) of the volume. 55

Figure 3.6: Imaging task with a cubic array of points (top) and Shepp-Logan phantom (bottom). The columns show the phantom, no matching layer, flat matching layer and convex matching layer reconstructions from left to right, respectively. The 25 x 25 mm xy, xz and yz planes through the centre of the imaging volume are shown from top to bottom for each reconstruction. All reconstruction cases were scaled identically. 56

Figure 4.1: Emission profile of two point sources as a function of the azimuthal and elevation angles. 63

Figure 4.2: Visual depiction of two methods to determine the angular acceptance of a transducer implemented in this work. The point source was moved along the solid line in the direction shown by the arrow. (a) Raster scanning methodology used in Chapter 2 which required distance correction while (b) was implemented in Chapter 3 and maintained a fixed distance between the transducer and point source at all times. Images are not to scale. 65

Figure 4.3: Transducer angular acceptance. (a) Figure 2.1 (d) shown again for comparison purposes where the red diamonds show experimental data and the blue line shows the mathematical model used in the simulated model of the system. (b) Example of the angular acceptance of another transducer from the PA array where red diamonds indicate experimentally collected data points from planes between 4 and 5 cm away from the transducer face. 66

Figure 4.4: Three transducers with (a) no matching layer, (b) a flat epoxy matching layer, and (c) a convex epoxy matching layer, where epoxy is depicted in purple. 67

Figure 4.5: A photoacoustic imaging system design utilizing an acoustic reflector. Adapted from Huang et al. [13]. 69

Figure 4.6: Sensitivity map of the centre z plane of the imaging volume, where each side is 2.1 cm and the colour represents sensitivity to signals in that voxel. 71

List of Abbreviations and Symbols

1D, 2D, 3D	One, two, three dimensional
cm	Centimetre
DAQ	Data acquisition
dB	Decibel
FDA	Food and Drug Administration
FOV	Field of view
GHz	Gigahertz
H&E	Haematoxylin and eosin
ICG	Indocyanine green
IO	Imaging operator
MAE	Mean absolute error
MEMS	Microelectromechanical system
MB	Model-based
MHz	Megahertz
mm	Millimetre
ns	Nanosecond
PA	Photoacoustic
PAI	Photoacoustic imaging
PAT	Photoacoustic tomography
RFS	Radiofrequency spectroscopy
RS	Raman spectroscopy
s	Second
SNR	Signal-to-noise ratio
SSIM	Structural similarity
SVD	Singular value decomposition
μm	Micrometre
US	Ultrasound

Preface

This dissertation includes the work completed throughout the duration of my MSc degree at the University of Western Ontario and Lawson Health Research Institute.

Chapter 1 introduces the fundamental principles of photoacoustic imaging (PAI). Applications of PAI are presented along with reconstruction techniques, system components, and design considerations. This chapter concludes with the motivation and objectives of my work.

Chapter 2 and 3 are based on manuscripts in preparation for submission to peer-reviewed journals. Chapter 2 focuses on a simulated model of the photoacoustic transducer array and varying transducer directionality to increase the field of view. Chapter 3 explores increasing the angular acceptance of transducers with a shaped matching layer to be utilized as an acoustic lens.

Chapter 4 provides a general discussion and summary of the work. Future areas of study are proposed.

Chapter 1

1 Introduction

1.1 Background

Photoacoustic imaging (PAI) is a developing biomedical imaging modality which has roots as far back as 1880 when Alexander Graham Bell first observed the formation of sound waves following light absorption. This hybrid modality takes advantage of the benefits of both optical and acoustic imaging modalities. Optical imaging alone has a restricted penetration depth in tissue due to the scattering of light, with a mean free path of approximately 1 mm [1]. To achieve a high image resolution, it is ideal to only collect information from photons that have not undergone scattering, which limits optical imaging to a very shallow region. Acoustic waves have significantly lower attenuation in tissue than light, approximately 1 dB/cm/MHz [2]. By acquiring information through acoustic waves, the issue of scattered light is nearly eliminated. This results in an imaging modality which has the contrast of optical imaging with its resolution derived from ultrasound (US).

1.2 Applications

Photoacoustic imaging can be performed on the scale of a cell up to the size of an organ. Contrast is derived from the optical absorption within a target and different chromophores can be targeted by selecting specific wavelengths of light. This section will briefly review PAI biomedical applications on varying scales and utilizing contrast from several molecules of interest.

Two commonly targeted endogenous chromophores in PAI are haemoglobin and melanin. To image *in vivo* at significant depths the absorption ranges of molecules abundant in tissue such as water and lipids must be avoided. Haemoglobin and melanin both fall within what is known as the optical window, where water does not dominate the absorbance and the wavelength of light used can still penetrate into tissue. Haemoglobin is of particular interest as oxygenated and deoxygenated haemoglobin molecules express different optical absorption properties. The absorption coefficients of some common endogenous chromophores can be found in Figure 1.1. Because of their differing optical

properties, the two molecules can be differentiated using PAI. Multispectral imaging using two wavelengths of light capable of determining blood oxygenation levels has been implemented in both bench top and hand held devices by taking advantage of haemoglobin's optical properties [3][4][5]. Melanin is concentrated to specific regions of the body and as such is typically used for dermal applications [6].

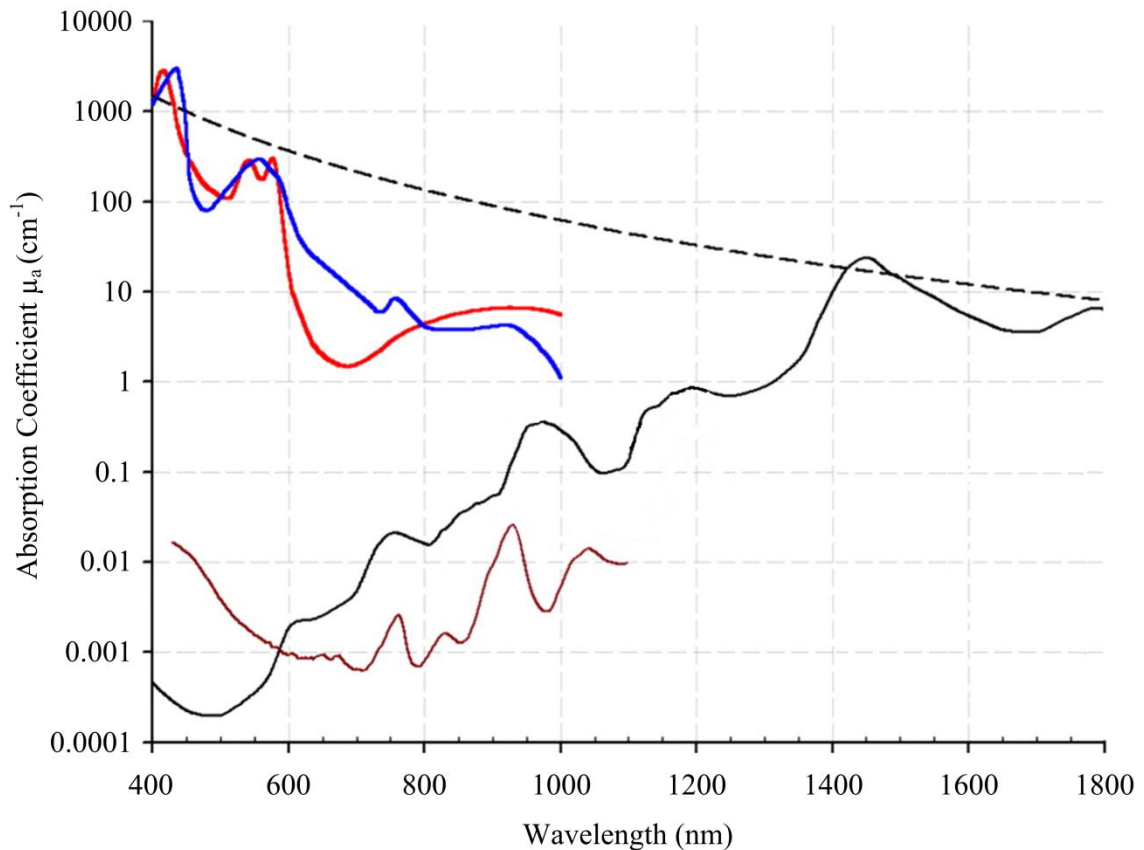


Figure 1.1: Absorption coefficient spectra of tissue chromophores, adapted from Beard et al. [7]. Water, solid black line; oxyhaemoglobin, red line; deoxyhaemoglobin, blue line; melanin, black dashed line; lipid, brown line.

Exogenous contrast can also be used for PAI and several contrast agents have been developed for this purpose. Palladium nanosheets, organometallic carbonyl clusters and gold nanosphere encapsulated nanoemulsions have all been developed as PAI contrast agents in recent years, with the former two already being tested *in vivo* [8][9][10]. Organic dyes such as indocyanine green (ICG) and methylene blue are used

clinically in applications such as lymph node tracking but have been used primarily in phantoms for PAI [11][12][13].

Using the aforementioned endogenous or exogenous contrast agents, PAI has been performed *in* and *ex vivo* and on scales from microscopy to whole breast imaging. Microscopy applications have been used to image microvasculature, melanoma and red blood cells [14][15]. Small animal imaging systems have been developed and used to acquire both functional and anatomical mouse images [16][17][18]. Breast imaging has been performed by several groups and systems have been designed for breast cancer detection [19][20][21]. The details of how PAI is accomplished will be described throughout the chapter.

1.3 Photoacoustic imaging theory

Photoacoustic imaging generally utilizes short laser pulses to illuminate an object of interest. Some of the laser energy is absorbed by the object and converted to heat, raising the temperature on the order of millikelvin [22]. The temperature increase results in thermoelastic expansion and an acoustic wave to be generated at the location of the absorber. The pressure wave propagates through a coupling medium, such as water, and is collected by ultrasound transducers. The information inherent in the photoacoustic waves is used to reconstruct images. The information in the following sections (1.3.1 and 1.3.2) is adapted from “Biomedical Optics: Principles and Imaging”, L. Wang and H. Wu, 2007.

1.3.1 Photoacoustic wave generation

In order for a photoacoustic wave to be produced, two conditions must be met: the thermal and stress relaxation times. Thermal relaxation time indicates the time required for heat to dissipate away from a directly-heated region. It can be described as

$$\tau_{\text{th}} = \frac{d_c^2}{\alpha_{\text{th}}} \quad (1.1)$$

where d_c is the characteristic dimension of the heated region and α_{th} is the thermal diffusivity. The stress relaxation time relates to the physical characteristics of the object

and the time taken to reach equilibrium after a stress has been applied. Stress relaxation is described as

$$\tau_s = \frac{d_c}{v_s} \quad (1.2)$$

where v_s is the speed of sound in the medium. In PAI the stress relaxation time is typically smaller than the thermal relaxation time and is the limiting confinement for PA wave generation. This time is generally a fraction of a microsecond and thus nanosecond laser pulses are often used in PAI, as energy from the laser pulse must be absorbed in a shorter period of time than it takes for the heat or stress to dissipate into surrounding tissues to produce a PA wave.

If the thermal and stress confinements are met, the associated pressure change is

$$p = \frac{\beta v_s^2 \mu_a F}{C_p} = \Gamma \mu_a F \quad (1.3)$$

where β is the thermal coefficient of volume expansion, μ_a is the optical absorption coefficient, F is the optical fluence, C_p is the specific heat capacity at constant pressure, and Γ is the Grueneisen parameter.

1.3.2 Photoacoustic wave propagation

After generation of the pressure wave as described in section 1.2.1, the photoacoustic wave propagates through a coupling medium such as water or saline to transducers. The pressure profile of the photoacoustic wave as a function of time at a point, r , will be bipolar. The pressure from a homogeneous optically absorbing sphere of radius R_s can be represented mathematically as

$$p(\tau) = \frac{\tau \mu_a F}{2r} \begin{cases} -v_s \tau, & |v_s \tau| \leq R_s \\ 0, & |v_s \tau| > R_s \end{cases} \quad (1.4)$$

where $\tau = t - r/v_s$ and is the time of flight of the pressure wave at location r and time t . The amplitude of the PA wave will be proportional to the absorption properties and laser fluence incident on the object. The width of the pressure wave indicates the size of the absorber and the time of flight indicates the distance of the absorber from the detecting transducer. These parameters are shown in Figure 1.2.

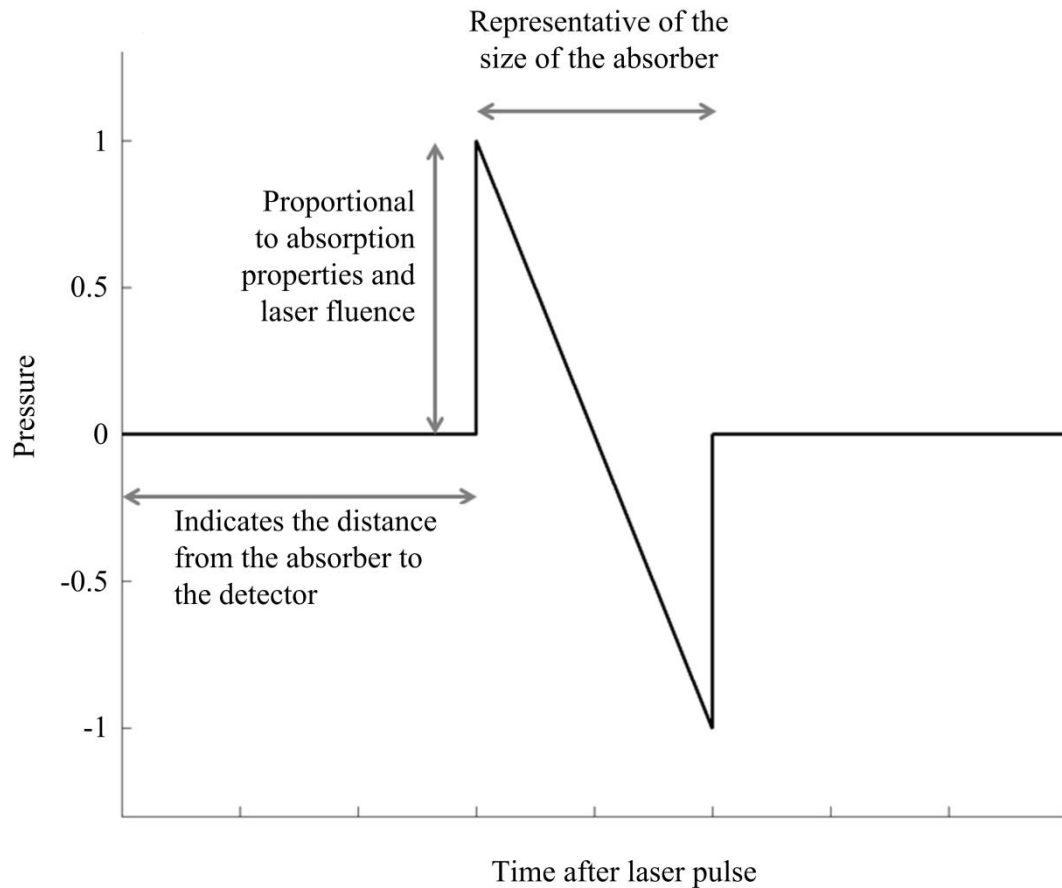


Figure 1.2: Pressure profile of a theoretical photoacoustic wave in the time domain.

1.4 Imaging methods

After photoacoustic wave generation and propagation, the pressure waves are detected, pre-amplified and converted from analog to digital information by a data acquisition system (DAQ). Photoacoustic transducers will be described in more detail in section 1.5.1. After data acquisition, signal processing may be performed. This may include band pass filtering, denoising signal, and averaging the signal from more than one laser pulse [23][24][25]. These processes are generally performed to remove noise and improve the signal-to-noise ratio (SNR).

Image reconstruction from the acquired data can be performed using several methodologies, including series solutions, back-projection algorithms, time reversal methods or model-based (MB) algorithms [23]. Each method of image reconstruction seeks to determine the initial pressure distribution, but approaches the problem in a

different way. Series solutions and back-projection algorithms aim to solve the problem analytically, while MB algorithms focus on a numerical solution.

Model-based algorithms require a significant memory load on computing devices compared to the analytical approximations of the solution [26]. However, the MB reconstruction is capable of accounting for experimental imperfections that cannot be considered in analytical models [23]. The MB method is becoming more accessible as computing technology advances and large memory banks become more affordable.

The MB linear model can be expressed mathematically as

$$\mathbf{g} = \mathbf{H}\mathbf{f} + \mathbf{e} \quad (1.5)$$

where \mathbf{g} is the measured data set, \mathbf{H} is the imaging operator (IO), \mathbf{f} is a representation of the absorber and \mathbf{e} is noise. The IO contains the response of each transducer to signal from each voxel within the imaging volume. Several photoacoustic point sources have been developed by different groups for characterization of PAI systems and our group has previously used a point source to capture the IO of the system [27][28][16]. In order to perform image reconstruction, the IO for the system must be captured and the pseudoinverse of \mathbf{H} calculated in order to solve for \mathbf{f} . \mathbf{H} can be decomposed by singular value decomposition (SVD) as described by

$$\mathbf{H} = \mathbf{U}\mathbf{S}\mathbf{V}^T \quad (1.6)$$

where \mathbf{U} is an $M \times M$ matrix, \mathbf{V} is an $N \times N$ matrix, and \mathbf{S} is an $M \times N$ diagonal matrix with entries representing the singular values of the imaging operator. The pseudoinverse of \mathbf{H} is then

$$\mathbf{H}^\dagger = \mathbf{V}\mathbf{S}^\dagger\mathbf{U}^T \quad (1.7)$$

where \mathbf{S}^\dagger is found by taking the reciprocal of each non-zero entry above a threshold on the diagonal of \mathbf{S} . In previous work, experimental reconstructions have utilized regularization such that singular values associated with an index greater than 20% of the matrix rank index were used in order to avoid null space singular vectors and noise [28]. Although capturing the IO and calculating the pseudoinverse are computationally demanding, they need only be calculated once for a unique experimental PAI system.

1.5 System design

Photoacoustic imaging systems incorporate many components including a minimum of: a light delivery system, transducer, DAQ and computer for reconstruction. The combinations of these components are nearly endless, allowing for PAI optimized for particular uses. The PAI system utilized by our group

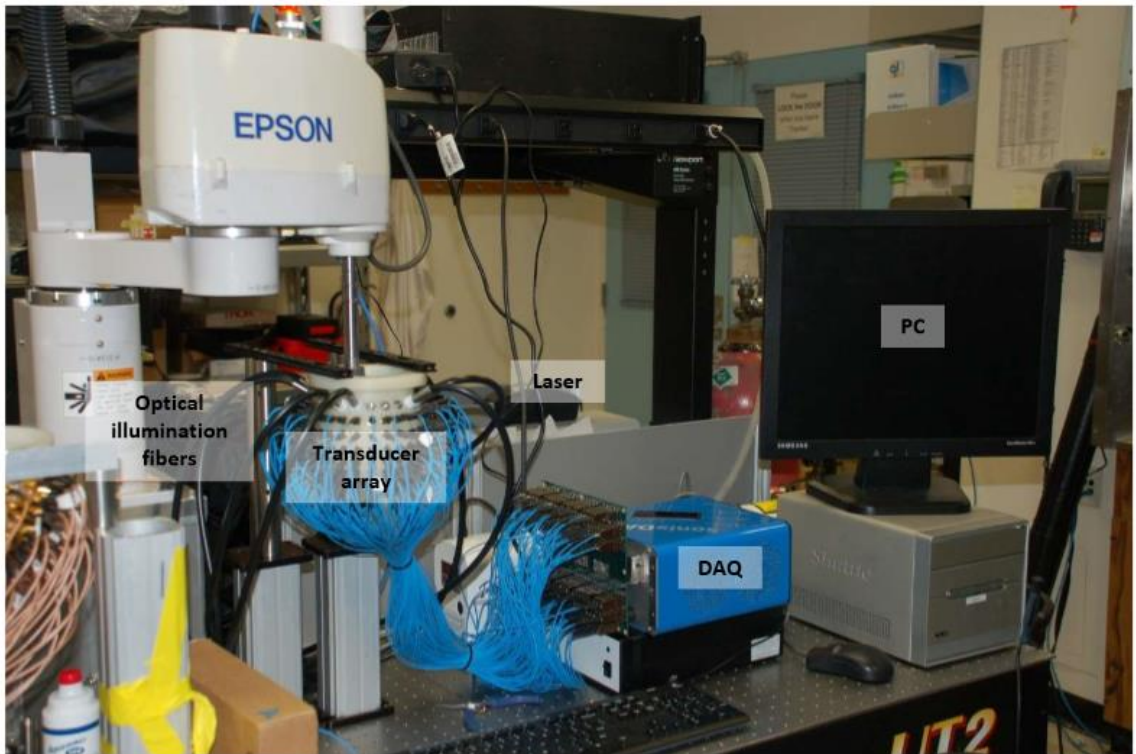


Figure 1.3: Photograph of the photoacoustic imaging system, with the laser source, optical illumination fibers (black fibers), transducer array, data acquisition (DAQ) system and personal computer (PC) indicated with labels.

This thesis will focus primarily on the transducers used to acquire PA waves; transducer type, characteristics, arrangement in arrays, scanning patterns and the resultant system.

1.5.1 Transducers for photoacoustic wave detection

The most common type of sensor used in PAI is based on piezoelectric elements [23]. Capacitive micromachined ultrasonic transducers and optical based sensors such as interferometers and resonators have also been utilized, although their use is less wide-

spread [29][30][31][32]. When designing and manufacturing or selecting piezoelectric transducers, the frequency, bandwidth, size and aperture must be taken into consideration. Because information about the size of the optical absorber is contained in the frequency of the signal, the frequency detection capabilities of the transducer select what size of absorbers it can resolve. Up to GHz transducers are used for photoacoustic microscopy while photoacoustic tomography (PAT) generally uses transducers on the order of 2-5 MHz, enabling sub-millimeter resolution [22][15][7]. To allow detection of a large range of absorber sizes, transducers used in PAI ideally have a very large bandwidth. Xu et al. found that the highest obtainable spatial resolution of a transducer approximates to between $0.6\lambda_c$ and $0.8\lambda_c$, where λ_c is the wavelength at the high cutoff frequency [33].

The aperture of the transducers contributes to the angle over which signals can be detected. The half-angle beam divergence (γ) at -6 dB for disc-shaped transducer elements can be expressed as

$$\gamma = \sin^{-1} \left(\frac{0.51\lambda}{D} \right) \quad (1.8)$$

where λ is the wavelength and D is the diameter of the transducer element [34].

Theoretically, the beam divergence of the pressure wave in the far field can also describe the detection pattern of the transducer [35]. It therefore follows that as the diameter of the PA transducer element increases, the acceptance angle of the transducer will decrease. An ideal transducer would be able to detect signals in a large volume in order to reconstruct a large region or necessitate less movement of the transducer to sample the region of interest. However, smaller transducer elements tend to be less sensitive and thus alternative approaches have been explored to increase the angular acceptance. Acoustic lenses are one of the more prevalent methods utilized, and have been shown to effectively increase the acceptance of transducers in PAI [35]. Xia et al. were able to increase the acceptance of a 1 MHz transducer from 20° to over 50° using a convex acrylic lens [36].

In addition to contributing to the acceptance of the transducer, the diameter of the piezoelectric element limits how closely transducers can be placed next to each other.

This has implications in the field of view and resolution of the system, and may contribute to scanning parameters, which will be discussed in the following sections.

Different approaches have been taken for the manufacturing of PAI transducers. Commercial transducers are available due to their use in ultrasound [37][38][39]. However, the requirements of PAI and US transducers differ and thus transducers designed specifically for PAI have also been manufactured [40]. Photoacoustic transducers tend to a greater broadband frequency response than their US counterparts and are passive – they need not create pressure waves, only receive them [41][42].

1.5.2 Transducer arrangement and scanning patterns

Photoacoustic imaging systems have been developed with a multitude of transducer arrangements and scanning or staring positions. Only one transducer is necessary to perform PAI; systems containing only a single US transducer have acquired whole-body images of zebrafish as well as acquired structural and functional images of a rat brain *in vivo* [39][43]. In PA microscopy, one transducer can be raster scanned to acquire images from the A-line data. A representation of this configuration is shown in Figure 1.3 (a). Yao et al. used a single US transducer to visualize oxygen metabolism in mouse microvasculature using a raster scanning methodology [44].

Multiple transducers can be placed side by side to create an array, increasing the size of the image and/or decreasing scanning time. Arrays are generally designed as a row (Figure 1.3 (b)) or grid spacing of transducers. Transducer arrays manufactured for US imaging are typically linear, with one line of transducer elements in a straight line or one transducer scanning on a 1D line to approximate the aforementioned [45]. For example, Xia et al. manufactured a custom linear transducer array for the purpose of breast imaging [40]. Linear arrays are typically scanned in a rectilinear, circular or combination pattern, often dependent on the imaging application. Accessibility and location of the object of interest may dictate the scanning pattern; Ermilov et al. used a linear scanning pattern in order to image vasculature in the forearm of a human [46]. Arc-shaped (Figure 1.3 (c)) and circular or ring transducer arrays are also common, where transducers are placed in a line that follows a curved path, forming a circle or forming a circle segment. Annular arrays are often translated perpendicularly to the array

orientation for the largest regional coverage. Ring arrays have been used for whole-body mouse imaging among other applications [47].

Following from arc and ring arrays, three-dimensional transducer arrangements also conform to spherical geometries. Arranging transducers in three dimensions allows for faster imaging as a larger solid angle can be sampled without translating or rotating the transducers. If scanning is performed, spherical or hemispherical arrays are typically rotated to capture information otherwise lost to the space between transducers (Figure 1.3 (d)) [48]. Although higher sampling can decrease artifacts and avoid resolution degradation by enabling larger solid angle coverage, it also increases the acquisition time [49]. Photoacoustic imaging systems focused on video frame rate image reconstruction tend to use transducer arrays which are stationary throughout imaging, called staring arrays. The resolution, acquisition time and field of view as a result of transducer array configuration will be discussed in more detail in the following section. Staring arrays have been used for multispectral PAI as well as functional imaging of the mouse brain [5][16].

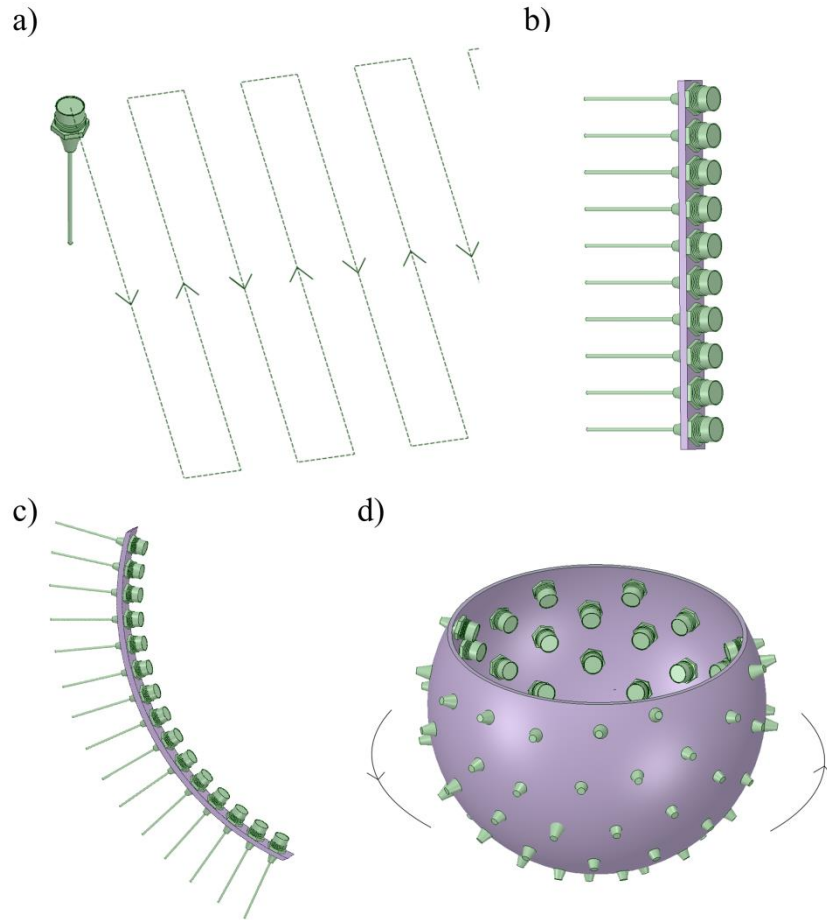


Figure 1.4: Transducer orientations. (a) A single transducer showing a raster scanning movement, (b) a linear array of transducers, (c) an arc array of transducers and (d) a spherical array of transducers showing a rotational movement.

1.5.3 Transducer-dependent system properties

Just as photoacoustic transducers have inherent properties such as frequency, bandwidth and aperture, PAI systems and the images taken by them can be described by their resolution, field of view, the wavelength used, penetration depth, laser repetition rate and the acquisition time for images, among others. This section will focus on the resolution, field of view and acquisition time of 3D PAI systems, which are largely dependent on the PA transducers used. As discussed previously, the resolution of the system will be limited by the finite bandwidth of the transducers utilized. The effective resolution of the system is also limited by the transducer array in that streaking artifacts are present in under-sampled reconstructions [23][50]. In order to decrease artifacts and

increase image quality, sampling should be performed to complete as much of the solid angle around the object of interest as possible. Kruger et al. used a 128 hemispherical transducer array scanned through 240 angles to obtain 64 x 64 mm² images of the breast with sub-millimeter resolution to a depth of 40 mm [19]. The 240 projections took 24 s to acquire. To decrease acquisition time, the number of transducers can be increased or the volume can be sampled more sparsely.

Video rate 3D PAI has been implemented by Buehler et al. using a 256 channel system in a spherical arrangement covering a solid angle of 240° in the azimuthal and 75° in the zenith directions [51]. A beating mouse heart was imaged at 10 frames/second with a FOV of 16 x 16 x 8 mm. The transverse resolution of the system was distance dependent and ranged from 200 to 800 μm from 0 to 10 mm away from the transducers. It can be seen that the acquisition time of the system can be decreased significantly but the FOV of the system has been greatly reduced in these two cases.

In another system developed by Wang et al., rat epilepsy was imaged *in vivo* at 3.3 frames/second with a 3:1 multiplexed 64 channel system [16]. The transducers were positioned in a staring spherical array and achieved a resolution of approximately 0.2 mm with a FOV of 20 x 20 x 4.5 mm. It is apparent that there is currently a limit on the FOV for fast-rate 3D PAI systems.

The FOV for a transducer array is accumulated from the individual FOVs of each transducer within the array, as represented in Figure 1.4. The FOV can be increased by increasing the size of the array – allowing the cone corresponding to the sensitivity of each transducer to be broadened where the object of interest is. This method poses challenges as the volume of coupling medium used in the spherical array will drastically increase with increasing sphere size. All of the systems described here have transducers which are directed towards the centre of the array. In order to increase the FOV the direction of each transducer can be altered to potentially increase the volume in which the individual FOVs converge. This strategy is the basis for Chapter 2. Another approach is to increase the FOV of each transducer, as outlined in section 1.5.1. This strategy is explored in Chapter 3, utilizing a matching layer as an acoustic lens.

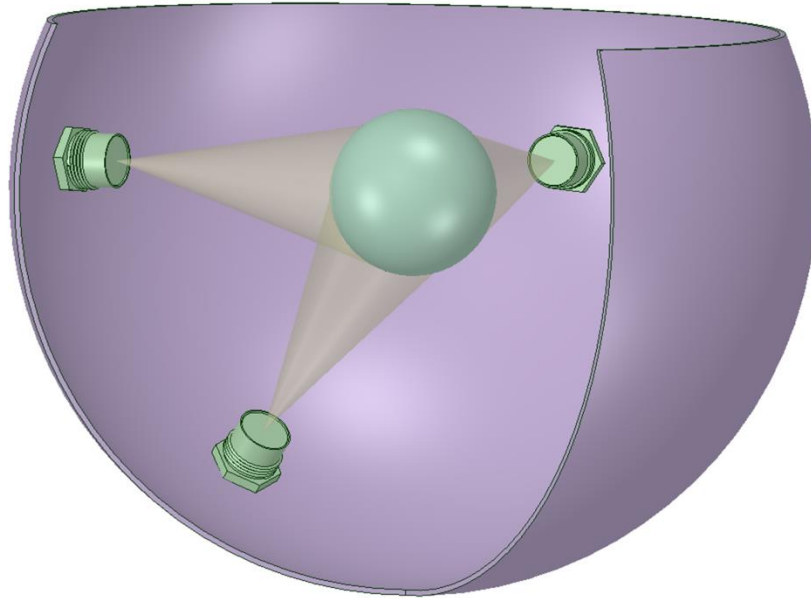


Figure 1.5: Representation of the field of view of a spherical transducer array. Three transducers are shown with their respective field of views contributing to the field of view of the array (green sphere).

1.6 Advanced methods for assessing system performance

While each photoacoustic system can be assessed by the sensitivity, resolution, apparent image quality and information it provides, more advanced measures of system performance have been developed and offer a quantitative evaluation of the system and the images it reconstructs. Our group has previously used methods based on the crosstalk matrix and SVD [52][28].

1.6.1 Crosstalk matrix

The crosstalk matrix, developed by Barrett et al., quantifies the system sensitivity and aliasing using the imaging operator. The crosstalk matrix was originally used in the Fourier domain and has been applied to photon emission tomography (PET) [53]. The method has been extended outside of the frequency domain and has been applied to wavelets for the assessment of shift-variant imaging systems [54]. Our group has previously used the crosstalk matrix in the spatial domain for system assessment [52]. The crosstalk matrix, \mathbf{B} , can be computed from

$$\mathbf{B} = \mathbf{H}\mathbf{H}^T \quad (1.9)$$

and each element in \mathbf{B} is given as

$$\mathbf{B}_{jj'} = \sum_{k=1}^K (\mathbf{H}_{jk} \mathbf{H}_{j'k}^T) \quad (1.10)$$

where \mathbf{H}^T is the transpose of \mathbf{H} , j and j' are the indexes of the voxel coefficients, k is the product of the time index for a transducer and the index of that transducer, and K is the product of the total number of indices and total transducers.

Two main measures can be obtained from the crosstalk matrix: sensitivity and aliasing. The sensitivity of the system can be found in the diagonal of the crosstalk matrix and is the product of the signal in a particular voxel multiplied by itself. This results in a scalar value that indicates the PA signal magnitude correlated with a particular voxel in the imaging volume. The aliasing of each voxel in the imaging volume is quantified in the rows of the crosstalk matrix; the overlap between signals from different voxels is quantified in each of the off-diagonal elements in the matrix. Any overlap between time series in two independent voxels indicates that these voxels cannot be distinguished from one another. For example, \mathbf{B}_{58} contains the multiplication of the fifth and eighth voxel's time series together which assigns a value to the intersection between the two signals.

1.6.2 Signal fidelity measures

The sensitivity and aliasing acquired from the crosstalk are valuable, but they are limited in proposing how to optimize the system and may not be fair evaluations between systems. For this reason, system performance metrics such as the mean absolute error (MAE) and structural similarity index (SSIM) have been used to objectively assess the crosstalk matrix [55]. MAE measures the similarity (or conversely, differences) of two sources. The mean absolute error (MAE) can be found according to

$$\text{MAE} = \frac{1}{n} \sum_{t=1}^n |e_t|^2 \quad (1.11)$$

where e_t is the estimated error. To evaluate the system, the MAE between the crosstalk matrix and the identity matrix was calculated. The identity matrix represents the ideal case, where the diagonal (sensitivity) is at 100% across the volume and the off-diagonal (aliasing) between voxels is zero.

The structural similarity index (SSIM) is a measure of perceived visual quality. While MAE does not take into account the spatial or temporal relationship between signals, SSIM has been used to assess video quality and has been adapted for 3D imaging applications [56][57]. SSIM can be applied to indicate the representative similarity between the sample and ideal case that is closer to the human perception of the image. The SSIM can be found using

$$SSIM(x, y) = \frac{(2\mu_x\mu_y + C_1)(2\sigma_{xy} + C_2)}{(\mu_x^2 + \mu_y^2 + C_1)(\sigma_x^2 + \sigma_y^2 + C_2)} \quad (1.12)$$

where μ is the average, σ is the covariance, σ^2 is the variance, subscript x denotes the ideal case, subscript y denotes the case to be compared, and C_1 and C_2 are constants [56].

1.7 Motivation and Objectives

The work in this thesis has been motivated by the restrictive field of view of real-time 3D photoacoustic imaging systems. As outlined in section 1.6, the size of objects capable of being imaged by staring transducer arrays has been limited to 2 or 3 cm with limited resolution in some of these cases [16][58]. Photoacoustic imaging has previously been used in breast imaging and by increasing the effective FOV of the system, PAI can be investigated as a tool to rapidly evaluate surgical lumpectomy specimens which are currently too large to be imaged [59][60][19].

I hypothesize that the sensitive volume of a staring photoacoustic transducer array can be made more uniform (thus increasing the field of view) as measured by the crosstalk matrix by i) directing transducer away from the centre of the array, and ii) utilising a shaped matching layer as an acoustic lens to increase the angular acceptance of individual transducers.

1.7.1 Lumpectomy margin assessment in the operating room

A lumpectomy procedure is commonly performed in conjunction with radiation and/or chemotherapy for the treatment of breast cancer. A lumpectomy entails removing the tumour and a small amount of surrounding tissue, deemed the margins. After excision, the surgical sample is sent for pathological testing to ensure that no cancerous tissues are present within the margins. Patients typically wait on the order of several weeks for results. If the margins are positive for cancerous tissue, this indicates that the

entire tumour was not removed and a re-excision surgery is required to remove any remaining tumour tissue. Attaining negative margins has been documented as the most significant predictor to avoid local recurrence, and the risk of local recurrence increases with the number of re-excisions that need to be performed [61][62]. Currently, 20 – 40% of patients require re-excision surgeries, postponing further treatment and increasing their risk of local recurrence [63]. A method for margin assessment in the operating room (OR) would allow surgeons to immediately remove additional tissues if margins are positive. By removing the tissue immediately, re-excision surgeries can be reduced – improving patient outcomes and reducing the load on the healthcare system.

To address this opportunity for improvement, primarily optical imaging technologies have been explored thus far. This is likely due to their relatively low cost compared to other imaging modalities and the ability to rapidly image with high sensitivity. A device called MarginProbe™ received premarket approval by the United States Food and Drug Administration (FDA) in December 2012. MarginProbe has been available in Europe since 2008 and is currently available in select regions in the United States. Manufactured by Dune Medical Devices, the MarginProbe utilizes radiofrequency spectroscopy (RFS) to determine if breast lumpectomy samples contain normal or malignant tissue. The device outputs a positive or negative reading. In a recent randomized trial, the surgeon acquired 30 – 50 measurements for each lumpectomy specimen and removed additional tissue from the surface of the lumpectomy cavity corresponding to any device-identified positive margins. The proportion of patients requiring a reexcision surgery was reduced to 19.8%, compared to a rate of 25.8% without use of the MarginProbe [64].

Another spectroscopy-based method under investigation for margin assessment is Raman spectroscopy (RS). Raman spectroscopy has been shown capable of classifying several subtypes of breast cancer (invasive ductal carcinoma, ductal carcinoma *in situ*, fibroadenoma) and normal breast tissue with an overall accuracy of 99% [65]. In the operating room, RS has been shown to have potential for rapid lumpectomy margin assessment as demonstrated on a small sample of lumpectomy specimens [66]. However, both RFS and RS have small probe diameters (7 mm and 2 mm, respectively) and must

obtain many measurements to cover the surface of the sample, or sample the surface sparsely. In addition, RS is more cumbersome as all lights in the operating room must be turned off in order to obtain measurements.

Photoacoustic imaging has been investigated for *in vivo* early breast cancer detection as well as lumpectomy margin assessment [59][60][67]. A microelectromechanical system (MEMS) based PAI system has been shown to have potential for intraoperative lumpectomy margin assessment by mapping murine tumours in 3D before excision [60]. The images were used to determine the size, shape and orientation of tissue to be removed and resulted in measurements within 0.2 mm of those determined by post-operative haematoxylin and eosin (H&E) staining, currently the gold standard. This technique is currently limited by a stationary probe which is submerged in water and not applicable for human clinical procedures.

Rapid assessment of the entire surgical specimen would be an improvement over other techniques currently under development for lumpectomy margin assessment. A PAI system utilizing a stationary transducer array should be capable of imaging an entire lumpectomy specimen at video-rate in order to determine the positive or negative status of the margins. Our group's current PAI system has a highly sensitive imaging volume up to approximately 1 x 1 x 1 cm, as discussed in Chapter 2. However, lumpectomy specimens are generally 4 – 6 cm in length and would not be compatible with the current system [68]. One hundred and twenty eight transducers were manufactured for utilization in a staring transducer array to conduct lumpectomy specimen imaging. The work in this thesis was performed in order to increase the field of view of the PAI system using the pre-manufactured transducers.

1.7.2 Objectives

This work aimed to increase the effective imaging volume of a photoacoustic imaging system by increasing the field of view of the staring transducer array. The first goal was to evaluate the effects of varying transducer directionality in a stationary transducer array on the performance of the photoacoustic imaging system. The second aim was to assess the effect of the matching layer shape on the angular acceptance of

photoacoustic transducers and the resulting consequences on imaging system performance.

1.7.3 Approach

To evaluate the effects of varying transducer directionality, a virtual replica of the existing photoacoustic transducer array was modeled. In order to mirror the physical system as closely as possible, the response of the array transducers was characterized and utilized in the model. A photoacoustic point source used to capture the imaging operator of the system was also characterized in order to reproduce the imaging operator and correct for any inhomogeneities in the point source emission. The imaging operator for a variety of transducer directionalities was acquired and the crosstalk matrix and associated performance metrics calculated. This determined if changing the directionality of transducers can increase the field of view of the array.

In order to assess the effect of the matching layer shape on the angular acceptance of photoacoustic transducers, the matching layer was varied from convex to concave. The matching layer curvature was quantified by acquiring a three-dimensional scan of the transducer face. The angular acceptance of each transducer was characterized and the correlation between matching layer curvature and angular acceptance was evaluated. A virtual model of the staring transducer array was used to predict the relative image quality when populating the array with transducers with no matching layer, a flat matching layer and a convex matching layer. These cases were assessed using signal fidelity measures applied to the crosstalk matrix and simulated imaging results.

1.8 References

- [1] J. Yao and L. V Wang, "Photoacoustic tomography: fundamentals, advances and prospects.," *Contrast Media Mol. Imaging*, vol. 6, no. 5, pp. 332–45, 2011.
- [2] M. Xu and L. V. Wang, "Photoacoustic imaging in biomedicine," *Rev. Sci. Instrum.*, vol. 77, no. 4, p. 041101, 2006.
- [3] Y. Sun, E. Sobel, and H. Jiang, "Noninvasive imaging of hemoglobin concentration and oxygen saturation for detection of osteoarthritis in the finger joints using multispectral three-dimensional quantitative photoacoustic tomography," *J. Opt.*, vol. 15, no. 5, p. 055302, May 2013.
- [4] A. Buehler, M. Kacprowicz, A. Taruttis, and V. Ntziachristos, "Real-time handheld multispectral optoacoustic imaging.," *Opt. Lett.*, vol. 38, no. 9, pp. 1404–6, May 2013.
- [5] I. Kosik and J. J. L. Carson, "Real-time multispectral 3-D photoacoustic imaging of blood phantoms," *Proc. SPIE*, vol. 8581, p. 85811V, Mar. 2013.
- [6] J. A. Viator, Ñ. J. Komadina, L. O. Svaasand, G. Aguilar, B. Choi, and J. S. Nelson, "A Comparative Study of Photoacoustic and Reflectance Methods for Determination of Epidermal Melanin Content," *J. Invest. Dermatol.*, vol. 122, no. 6, pp. 1432–1439, 2004.
- [7] P. Beard, "Biomedical photoacoustic imaging.," *Interface Focus*, vol. 1, no. 4, pp. 602–31, Aug. 2011.
- [8] L. Nie, M. Chen, X. Sun, P. Rong, N. Zheng, and X. Chen, "Palladium nanosheets as highly stable and effective contrast agents for in vivo photoacoustic molecular imaging.," *Nanoscale*, vol. 6, no. 3, pp. 1271–6, Jan. 2014.
- [9] K. V. Kong, L.-D. Liao, Z. Lam, N. V Thakor, W. K. Leong, and M. Olivo, "Organometallic carbonyl clusters: a new class of contrast agents for photoacoustic cerebral vascular imaging.," *Chem. Commun. (Camb)*, vol. 50, no. 20, pp. 2601–3, Mar. 2014.
- [10] C.-W. Wei, M. Lombardo, K. Larson-Smith, I. Pelivanov, C. Perez, J. Xia, T. Matula, D. Pozzo, and M. O'Donnell, "Nonlinear contrast enhancement in photoacoustic molecular imaging with gold nanosphere encapsulated nanoemulsions.," *Appl. Phys. Lett.*, vol. 104, no. 3, p. 033701, Jan. 2014.
- [11] M. Chu and Y. Wan, "Sentinel lymph node mapping using near-infrared fluorescent methylene blue," *JBIOSC*, vol. 107, no. 4, pp. 455–459, 2009.

- [12] I. Kosik and J. J. L. Carson, "Combined 3D photoacoustic and 2D fluorescence imaging of indocyanine green contrast agent flow," *Proc. SPIE*, vol. 8581, p. 858143, Mar. 2013.
- [13] G. Ku and L. V Wang, "Deeply penetrating photoacoustic tomography in biological tissues enhanced with an optical contrast agent," *Opt. Lett.*, vol. 30, no. 5, pp. 507–9, Mar. 2005.
- [14] R. Bitton, R. Zemp, J. Yen, L. V Wang, and K. K. Shung, "A 3-D high-frequency array based 16 channel photoacoustic microscopy system for in vivo micro-vascular imaging," *IEEE Trans. Med. Imaging*, vol. 28, no. 8, pp. 1190–7, Aug. 2009.
- [15] M. Rui, S. Narashimhan, W. Bost, F. Stracke, E. Weiss, R. Lemor, and M. C. Kolios, "Gigahertz optoacoustic imaging for cellular imaging," *Proc. SPIE*, vol. 7564, pp. 756411–6, Feb. 2010.
- [16] B. Wang, L. Xiang, M. S. Jiang, J. Yang, Q. Zhang, P. R. Carney, and H. Jiang, "Photoacoustic tomography system for noninvasive real-time three-dimensional imaging of epilepsy," *Biomed. Opt. Express*, vol. 3, no. 6, pp. 1427–32, Jun. 2012.
- [17] D. R. Reinecke, R. A. Kruger, R. B. Lam, and S. P. Del Rio, "Co-registered photoacoustic, thermoacoustic and ultrasound mouse imaging," *Proc. SPIE*, vol. 7564, pp. 1–9, 2010.
- [18] J. Gamelin, A. Maurudis, A. Aguirre, F. Huang, P. Guo, L. V Wang, and Q. Zhu, "A real-time photoacoustic tomography system for small animals," *Opt. Express*, vol. 17, no. 13, pp. 10489–98, Jun. 2009.
- [19] R. A. Kruger, R. B. Lam, D. R. Reinecke, S. P. Del Rio, and R. P. Doyle, "Photoacoustic angiography of the breast," *Med. Phys.*, vol. 37, no. 11, 2010.
- [20] V. Nadvoretzkiy, S. Ermilov, H. Brecht, R. Su, and A. Oraevsky, "Image processing and analysis in a dual-modality optoacoustic / ultrasonic system for breast cancer diagnosis," *Proc. SPIE*, vol. 7899, no. 713, pp. 1–6, 2011.
- [21] W. Xia, D. Piras, M. K. a Singh, J. C. G. van Hespén, T. G. van Leeuwen, W. Steenbergen, and S. Manohar, "Design and evaluation of a laboratory prototype system for 3D photoacoustic full breast tomography," *Biomed. Opt. Express*, vol. 4, no. 11, pp. 2555–69, Jan. 2013.
- [22] V. Ntziachristos, J. Ripoll, L. V Wang, and R. Weissleder, "Looking and listening to light: the evolution of whole-body photonic imaging," *Nat. Biotechnol.*, vol. 23, no. 3, pp. 313–20, Mar. 2005.

- [23] C. Lutzweiler and D. Razansky, "Optoacoustic imaging and tomography: reconstruction approaches and outstanding challenges in image performance and quantification.," *Sensors (Basel)*, vol. 13, no. 6, pp. 7345–84, Jan. 2013.
- [24] S. H. Holan and J. a Viator, "Automated wavelet denoising of photoacoustic signals for circulating melanoma cell detection and burn image reconstruction.," *Phys. Med. Biol.*, vol. 53, no. 12, pp. N227–36, Jun. 2008.
- [25] Z. Ren, G. Liu, Z. Huang, W. Zeng, and D. Li, "Laser-induced photoacoustic glucose spectrum denoising using an improved wavelet threshold translation-invariant algorithm," *Int. Symp. Photoelectron. Detect. Imaging 2009 Laser Sens. Imaging*, vol. 7382, p. 73822R–73822R–8, Jul. 2009.
- [26] M. A. Araque Caballero, J. J. Gateau, X.-L. Dean-Ben, V. Ntziachristos, M. Ángel, and A. Caballero, "Model-based optoacoustic image reconstruction of large three-dimensional tomographic datasets acquired with an array of directional detectors.," *IEEE Trans. Med. Imaging*, vol. 33, no. 2, pp. 433–43, Feb. 2014.
- [27] R. a. Kruger, W. L. Kiser, D. R. Reinecke, and G. a. Kruger, "Thermoacoustic computed tomography using a conventional linear transducer array," *Med. Phys.*, vol. 30, no. 5, p. 856, 2003.
- [28] M. Roumeliotis, R. Z. Stodilka, M. a Anastasio, E. Ng, and J. J. L. Carson, "Singular value decomposition analysis of a photoacoustic imaging system and 3D imaging at 0.7 FPS.," *Opt. Express*, vol. 19, no. 14, pp. 13405–17, Jul. 2011.
- [29] B. Chen, F. Chu, X. Liu, Y. Li, J. Rong, and H. Jiang, "AlN-based piezoelectric micromachined ultrasonic transducer for photoacoustic imaging," *Appl. Phys. Lett.*, vol. 103, no. 3, p. 031118, 2013.
- [30] H. Li, B. Dong, Z. Zhang, H. F. Zhang, and C. Sun, "A transparent broadband ultrasonic detector based on an optical micro-ring resonator for photoacoustic microscopy.," *Sci. Rep.*, vol. 4, p. 4496, Jan. 2014.
- [31] R. W. Speirs and A. I. Bishop, "Photoacoustic tomography using a Michelson interferometer with quadrature phase detection," *Appl. Phys. Lett.*, vol. 103, no. 5, p. 053501, 2013.
- [32] A. Hochreiner, J. Bauer-Marschallinger, P. Burgholzer, B. Jakoby, and T. Berer, "Non-contact photoacoustic imaging using a fiber based interferometer with optical amplification.," *Biomed. Opt. Express*, vol. 4, no. 11, pp. 2322–31, Jan. 2013.
- [33] M. Xu and L. Wang, "Analytic explanation of spatial resolution related to bandwidth and detector aperture size in thermoacoustic or photoacoustic reconstruction," *Phys. Rev. E*, vol. 67, no. 5, p. 056605, May 2003.

- [34] R/D Tech Guildeline, *Introduction to Phased Array Ultrasonic Technology Applications*. Quebec: R/D Tech Inc., 2004, pp. 44–46.
- [35] A. Manuscript, “A Negative Lens Concept for Photoacoustic Tomography,” *Phys. Rev. E Stat. Nonlinear, Soft Matter Phys.*, vol. 78, 2008.
- [36] W. Xia, D. Piras, M. Heijblom, J. C. G. Van Hespén, S. Van Veldhoven, C. Prins, W. Steenbergen, T. G. Van Leeuwen, and S. Manohar, “Enlarged acceptance angle of a finite size detector in photoacoustic imaging using acoustic lenses,” *Proc. SPIE-OSA*, vol. 8090, pp. 80900L–1–7, Jun. 2011.
- [37] Z. Zhao, J. Hast, R. Myllylä, and M. Käsäkoski, “Pulsed photoacoustic measurements of suspensions: in case study of mitochondrial NADH and its phantom,” *Proc. SPIE*, vol. 7142, pp. 714213–714213–7, Sep. 2008.
- [38] R. a Kruger, D. R. Reinecke, and G. a Kruger, “Thermoacoustic computed tomography--technical considerations,” *Med. Phys.*, vol. 26, no. 9, pp. 1832–7, Sep. 1999.
- [39] R. Ma, M. Distel, X. L. Deán-Ben, V. Ntziachristos, and D. Razansky, “Non-invasive whole-body imaging of adult zebrafish with optoacoustic tomography,” *Phys. Med. Biol.*, vol. 57, no. 22, pp. 7227–37, Nov. 2012.
- [40] W. Xia, D. Piras, M. Heijblom, J. Van Hespén, S. van Veldhoven, C. Prins, T. G. van Leeuwen, W. Steenbergen, and S. Manohar, “A custom-made linear array transducer for photoacoustic breast imaging,” *Proc. SPIE*, vol. 8223, p. 82233D–82233D–6, Feb. 2012.
- [41] L. Xi, X. Li, and H. Jiang, “Variable-thickness multilayered polyvinylidene fluoride transducer with improved sensitivity and bandwidth for photoacoustic imaging,” *Appl. Phys. Lett.*, vol. 101, no. 17, p. 173702, 2012.
- [42] W. Xia, D. Piras, J. C. G. van Hespén, S. van Veldhoven, C. Prins, T. G. van Leeuwen, W. Steenbergen, and S. Manohar, “An optimized ultrasound detector for photoacoustic breast tomography,” *Med. Phys.*, vol. 40, no. 3, p. 032901, Mar. 2013.
- [43] X. Wang, Y. Pang, G. Ku, X. Xie, G. Stoica, and L. V Wang, “Noninvasive laser-induced photoacoustic tomography for structural and functional in vivo imaging of the brain,” *Nat. Biotechnol.*, vol. 21, no. 7, pp. 803–6, Jul. 2003.
- [44] J. Yao, K. I. Maslov, Y. Zhang, Y. Xia, and L. V Wang, “Label-free oxygen-metabolic photoacoustic microscopy in vivo,” *J. Biomed. Opt.*, vol. 16, no. 7, p. 076003, Jul. 2011.

- [45] S. a. Ermilov, M. P. Fronheiser, V. Nadvoretzky, H.-P. Brecht, R. Su, A. Conjusteau, K. Mehta, P. Otto, and A. a. Oraevsky, "Real-time optoacoustic imaging of breast cancer using an interleaved two-laser imaging system coregistered with ultrasound.," *Proc. SPIE*, vol. 7564, no. 713, p. 75641W–75641W–7, Feb. 2010.
- [46] S. A. Ermilov, H.-P. Brecht, M. P. Fronheiser, V. Nadvoretzky, R. Su, A. Conjusteau, and A. a. Oraevsky, "In vivo 3D visualization of peripheral circulatory system using linear optoacoustic array," *Proc. SPIE*, vol. 7564, no. 713, pp. 756422–756422–8, Feb. 2010.
- [47] J. Xia, M. Chatni, K. Maslov, and L. V. Wang, "Anatomical and metabolic small-animal whole-body imaging using ring-shaped confocal photoacoustic computed tomography," *Proc. SPIE*, vol. 8581, p. 85810K–85810K–6, Mar. 2013.
- [48] R. A. Kruger, R. B. Lam, D. R. Reinecke, S. P. Del Rio, R. P. Doyle, and S. P. Del Rio, "Photoacoustic angiography of the breast," *Med. Phys.*, vol. 37, no. 11, p. 6096, 2010.
- [49] M. Ángel, A. Caballero, J. Gateau, and V. Ntziachristos, "Model-Based Optoacoustic Image Reconstruction of Large Three-Dimensional Tomographic Datasets Acquired With an Array of Directional Detectors," *IEEE Trans. Med.*, vol. 33, no. 2, pp. 433–443, 2014.
- [50] R. Kruger, D. Reinecke, G. Kruger, M. Thornton, P. Picot, T. Morgan, K. Stantz, and C. Mistretta, "HYPR-spectral photoacoustic CT for preclinical imaging," *Proc. SPIE*, vol. 7177, p. 71770F–71770F–10, Feb. 2009.
- [51] a Buehler, X. L. Deán-Ben, J. Claussen, V. Ntziachristos, and D. Razansky, "Three-dimensional optoacoustic tomography at video rate.," *Opt. Express*, vol. 20, no. 20, pp. 22712–9, Sep. 2012.
- [52] M. Roumeliotis, R. Z. Stodilka, M. a Anastasio, G. Chaudhary, H. Al-Abed, E. Ng, A. Immucci, and J. J. L. Carson, "Analysis of a photoacoustic imaging system by the crosstalk matrix and singular value decomposition.," *Opt. Express*, vol. 18, no. 11, pp. 11406–17, May 2010.
- [53] R. Z. Stodilka, E. J. Soares, and S. J. Glick, "Characterization of tomographic sampling in hybrid PET using the Fourier crosstalk matrix.," *IEEE Trans. Med. Imaging*, vol. 21, no. 12, pp. 1468–78, Dec. 2002.
- [54] J. Qi, S. Member, and R. H. Huesman, "Wavelet Crosstalk Matrix and Its Application to Assessment of Shift-Variant Imaging Systems," *IEEE Trans. Nucl. Sci.*, vol. 51, no. 1, pp. 123–129, 2004.

- [55] P. Wong, “Three-dimensional Photoacoustic Tomography System Design Analysis and Improvement,” The University of Western Ontario, 2014.
- [56] Z. Wang, A. C. Bovik, H. R. Sheikh, E. P. Simoncelli, and S. S. Member, “Image quality assessment: from error visibility to structural similarity.,” *IEEE Trans. Image Process.*, vol. 13, no. 4, pp. 600–12, Apr. 2004.
- [57] K. Zeng and Z. Wang, “3D-SSIM for Video Quality Assessment,” *IEEE ICIP*, pp. 621–624, 2012.
- [58] P. Ephrat, M. Roumeliotis, F. S. Prato, and J. J. L. Carson, “Four-dimensional photoacoustic imaging of moving targets.,” *Opt. Express*, vol. 16, no. 26, pp. 21570–81, Dec. 2008.
- [59] S. A. Ermilov, T. Khamapirad, A. Conjuteau, M. H. Leonard, R. Lacewell, K. Mehta, T. Miller, and A. Oraevsky, “Laser optoacoustic imaging system for detection of breast cancer.,” *J. Biomed. Opt.*, vol. 14, no. 2, p. 024007, 2009.
- [60] L. Xi, S. R. Grobmyer, L. Wu, R. Chen, G. Zhou, L. G. Gutwein, J. Sun, W. Liao, Q. Zhou, H. Xie, and H. Jiang, “Evaluation of breast tumor margins in vivo with intraoperative photoacoustic imaging.,” *Opt. Express*, vol. 20, no. 8, pp. 8726–31, Apr. 2012.
- [61] T. S. Menes, P. I. Tartter, I. Bleiweiss, J. H. Godbold, A. Estabrook, and S. R. Smith, “The consequence of multiple re-excisions to obtain clear lumpectomy margins in breast cancer patients.,” *Ann. Surg. Oncol.*, vol. 12, no. 11, pp. 881–5, Nov. 2005.
- [62] M. C. Smitt, K. W. Nowels, M. J. Zdeblick, S. Jeffrey, R. W. Carlson, F. E. Stockdale, and D. R. Goffinet, “The importance of the lumpectomy surgical margin status in long-term results of breast conservation.,” *Cancer*, vol. 76, no. 2, pp. 259–67, Jul. 1995.
- [63] R. G. Pleijhuis, M. Graafland, J. de Vries, J. Bart, J. S. de Jong, and G. M. van Dam, “Obtaining adequate surgical margins in breast-conserving therapy for patients with early-stage breast cancer: current modalities and future directions.,” *Ann. Surg. Oncol.*, vol. 16, no. 10, pp. 2717–30, Oct. 2009.
- [64] F. Schnabel, S. K. Boolbol, M. Gittleman, T. Karni, L. Tafta, S. Feldman, A. Police, N. B. Friedman, S. Karlan, D. Holmes, S. C. Willey, M. Carmon, K. Fernandez, S. Akbari, J. Harness, L. Guerra, T. Frazier, K. Lane, R. M. Simmons, A. Estabrook, and T. Allweis, “A randomized prospective study of lumpectomy margin assessment with use of MarginProbe in patients with nonpalpable breast malignancies.,” *Ann. Surg. Oncol.*, vol. 21, no. 5, pp. 1589–95, May 2014.

- [65] S. K. Majumder, M. D. Keller, F. I. Boulos, M. C. Kelley, and A. Mahadevan-Jansen, "Comparison of autofluorescence, diffuse reflectance, and Raman spectroscopy for breast tissue discrimination.," *J. Biomed. Opt.*, vol. 13, no. 5, p. 054009, 2008.
- [66] A. S. Haka, Z. Volynskaya, J. a Gardecki, J. Nazemi, J. Lyons, D. Hicks, M. Fitzmaurice, R. R. Dasari, J. P. Crowe, and M. S. Feld, "In vivo margin assessment during partial mastectomy breast surgery using raman spectroscopy.," *Cancer Res.*, vol. 66, no. 6, pp. 3317–22, Mar. 2006.
- [67] R. A. Kruger, R. B. Lam, D. R. Reinecke, S. P. Del Rio, and R. P. Doyle, "Photoacoustic angiography of the breast," *Med. Phys.*, vol. 37, no. 11, p. 6096, 2010.
- [68] M. Singh, G. Singh, K. T. Hogan, K. a Atkins, and A. T. Schroen, "The effect of intraoperative specimen inking on lumpectomy re-excision rates.," *World J. Surg. Oncol.*, vol. 8, no. February 2009, p. 4, Jan. 2010.

Chapter 2

2 Multi-directional staring array for photoacoustic imaging

This chapter is based on a manuscript currently being prepared for publication in a peer-reviewed journal. The work presented in this chapter aimed to increase the field of view of a photoacoustic imaging system by changing the directivity of transducers within a staring photoacoustic transducer array.

2.1 Introduction

2.1.1 Background

Photoacoustic (PA) imaging utilizes an incident laser pulse to induce ultrasonic emissions from optical absorbers within an object. The bipolar pressure waves produced by the thermoelastic process propagate through a coupling medium and are detected by transducers and used as the basis to reconstruct images of the absorbers [1]. The modality offers better penetration depth and resolution over direct optical imaging [2]. The advantages of photoacoustic imaging over other optical methods has motivated the development and utilization of the modality for biomedical applications such as whole-body small animal imaging [3][4], breast imaging [5][6], prostate imaging [7], characterization of vasculature [8] and microscopy [9][10].

2.1.2 Photoacoustic transducer arrays

Transducer arrays for PA imaging have been typically linear, annular, hemispherical or near-spherical in shape, which result in plane, cylindrical or spherical detection geometries, respectively [11]. Furthermore, transducer arrays have been used in either a scanning or a staring configuration. Scanning arrays contain one or more movable transducers, enabling the capture of information over small angular increments. Linear and annular arrays must be scanned to provide a 3D image. Staring arrays maintain a fixed position and allow high-speed two- or three-dimensional imaging since they do not need to be translated around the object [12][13]. The spherical or annular transducer arrays reported to date have transducers oriented toward the centre of the array [12][14][15][16][17]. While this allows for optimal signal detection from the centre of

the array, the signal detection sensitivity drops off rapidly when measured radially from the centre of the array [18][19].

In the past, the majority of photoacoustic imaging systems have used scanning arrays and acquisition time has been sacrificed in lieu of a larger imaging volume. Systems that have accomplished real-time imaging are limited to 3D imaging in a narrow imaging volume typically less than 5 mm in thickness [12][16][20]. Systems capable of larger 3D imaging volumes take on the order of seconds to minutes to capture the data required for reconstruction [21][6]. Our group has previously demonstrated PAI for a reconstruction volume of 2 x 2 x 2 cm at 10 frames per second [22]. However, the ability of the system to detect photoacoustic signals from sources near the perimeter of the volume was suboptimal due to the limited angular acceptance of the transducer elements. Motivated by the need to image larger objects such as tissue specimens, but restricted by the availability of transducer elements with narrow angular acceptance, we investigated transducer arrangements with the intent of increasing the available reconstruction volume.

2.1.3 Objective and Approach

To increase the available reconstruction volume, our objective was to increase the uniformity of the overall system sensitivity within the transducer array. Transducer response in the object space was measured using a photoacoustic point-like source. This response was mathematically modeled and used to compute the response of a simulated version of the photoacoustic transducer array. The transducer array was varied by directing transducers at a cubic lattice of points throughout the image space. Two phantom imaging tasks were performed with the simulated systems to evaluate the effect of transducer directivity on image quality. System design was assessed using the sensitivity, aliasing, mean absolute error and structural sensitivity index.

2.2 Methods

2.2.1 Characterization of System Components

A photoacoustic point source similar to that in our previous work was utilized [18]. Briefly, the end of a 50- μm diameter optical fiber was polished and coated with

Black Connector Coating (MG Chemicals). The optical fiber was secured on a SCARA robot (Model E2C351A – UL, Epson) to facilitate scanning the fiber throughout the imaging volume.

The PA point source was characterized to determine its angular emission profile. A single transducer was used to measure the point source emission in the azimuthal and zenith directions at points equidistant from the source [23]. Photoacoustic point source emission was measured every 45° in the azimuthal direction and at ten angles in the zenith direction between 0° and 90° away from the axis of the transducer (Figure 2.1 (a) and (b)).

The PA imaging system utilized custom-built unfocused transducers with a central frequency of 2.7 MHz (~124% bandwidth) [22]. The distance dependence of the signal amplitude detected by the transducer was measured using the robot mounted point source. The point source was positioned directly in front of the transducer and scanned between 3 and 7 cm away from the transducer face in 1 mm increments (Figure 2.1 (c)). Signal amplitude was confirmed to be inversely proportional to the distance between the source and transducer. The angular acceptance of a transducer was measured by scanning the point source in a 3 cm straight line centered on the transducer and normal to the axis of the transducer face. The 8 scanning lines were between 1 and 8 cm away from the transducer face in 1 cm increments (Figure 2.1 (d)). All measurements to characterize the point source and transducers were completed at 1064 nm with 6 ns pulses and measurements were averaged between 6 pulses in each of three trials. The angle between the normal to the transducer face and where the point source was located was calculated. The angle and intensity of the signal from the source, corrected for distance, were plotted and fit to a curve.

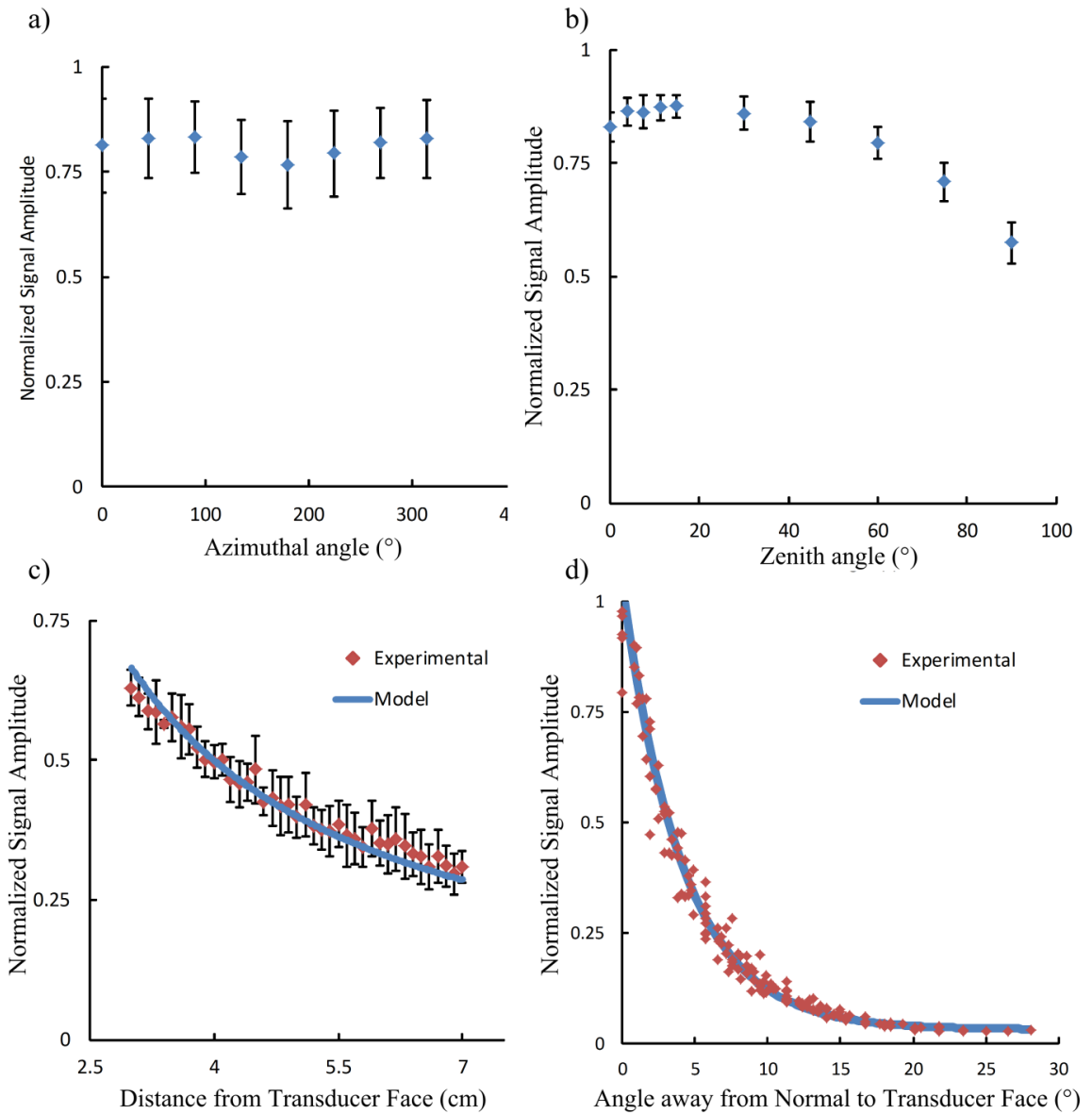


Figure 2.1: (a) Characterization of the photoacoustic point source along the azimuthal and (b) zenith directions. Each point is the mean of three trials with one standard deviation shown as error bars. (c) Pressure wave amplitude was measured as a function of distance from the transducer face, where each point is an average of three trials and one standard deviation above and below the mean is shown with error bars. An equation fitted to the data is shown as a blue line. (d) Normalized photoacoustic signal intensity shown as a function of the angle away from normal to the transducer face in degrees. Each point is independent and an equation fitted to the data is shown in blue.

2.2.2 Simulated Model of Photoacoustic Imaging System

A simulated approximation of the PA imaging system was designed in Matlab, with transducer locations shown in Figure 2.2 (c). The acquisition of the imaging operator, described by Roumeliotis et al. [19] was mimicked in the simulation by allocating a grid corresponding to the scan dimensions and accumulating the signal from a simulated photoacoustic point source for each transducer and each voxel of the volume. A representative signal produced by the 50- μm diameter fiber point source was produced by averaging 64000 signals from the source (Figure 2.2 (a)). This representative signal was scaled according to the distance and angle away from the transducer face. The response of a transducer as a function of the angle away from normal to the transducer face is shown in Figure 2.2 (b). The directionality of the transducers was varied by selecting between 8 and 125 points on a cubic lattice (Figure 2.2 (d)). These points are referred to as directional points. The directional points were evenly spaced on a cube centred in the array with sides ranging from 0 to 14 mm, where a 0 mm cube was equivalent to all transducers being directed towards the centre of the array. A nearly equal number of transducers were assigned to each directional point.

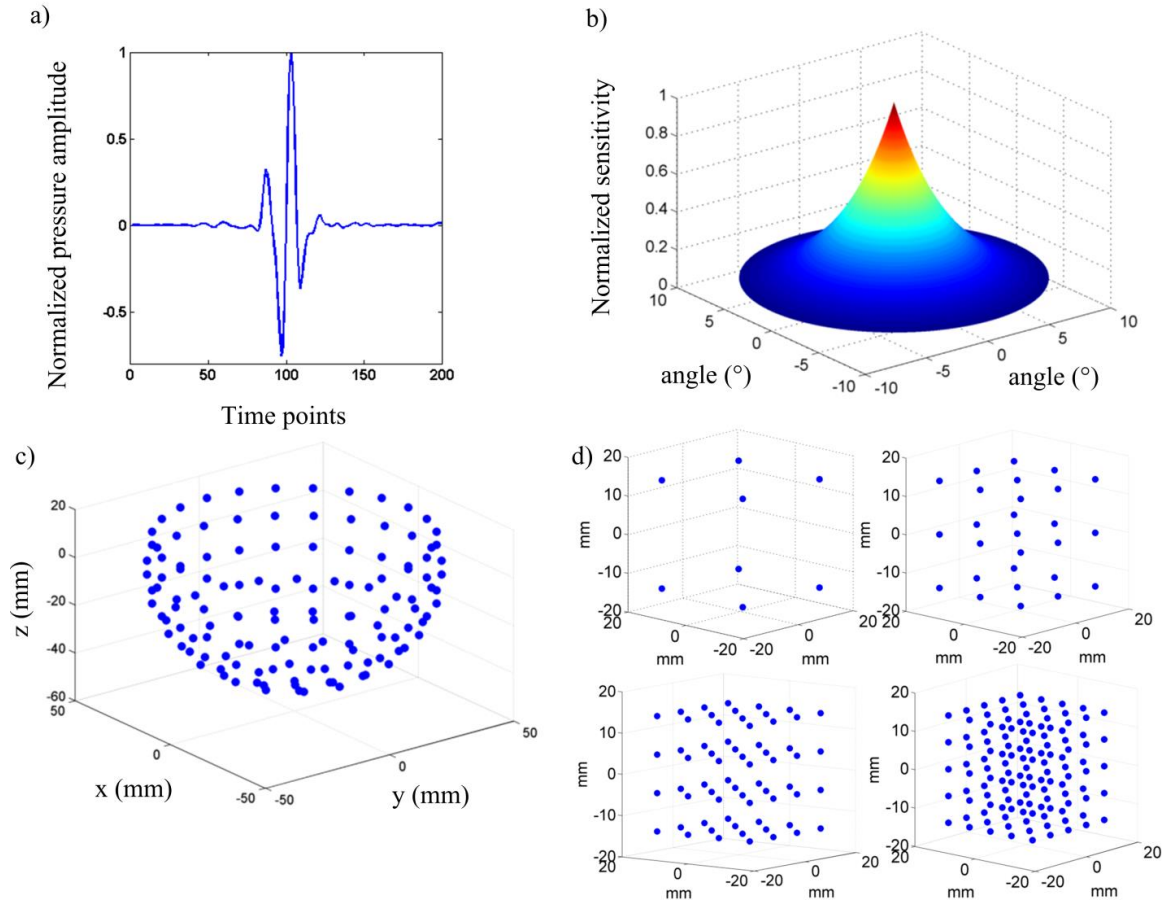


Figure 2.2: (a) Representative photoacoustic signal used for modeling system response. (b) Relative sensitivity of the representative transducer away from normal. (c) Point cloud representation of the 129 transducer locations in the stationary array. (d) Point cloud representation of 8, 27, 64 and 125 directional point locations, from left to right, top to bottom respectively, at 14 mm cube spacing.

2.2.3 Image reconstruction

Please refer to section 1.4 for image reconstruction techniques.

2.2.4 Imaging Experiment

Two phantoms were used for imaging assessment: a Shepp-Logan phantom and a grid of 343 50- μm diameter point sources in a $7 \times 7 \times 7$ formation within an 18 mm cube. The Shepp-Logan phantom code was obtained from MATLAB file exchange [25]. The pseudoinverse was calculated for each transducer directionality parameter using the QUIC-SVD method as described by Holmes et al. with 20% regularization of the singular

values [26]. The pseudoinverses were used to reconstruct the phantom by solving for f as described in Equation 2.2 with noise added at a signal-to-noise ratio of 10.

2.2.5 Evaluation methods

Please see section 1.6.1 for an explanation of the crosstalk matrix.

The crosstalk matrix was calculated according to Equation 1.9 for each of the transducer directionality parameters. The diagonal of the crosstalk matrix was reshaped to reflect the geometry of the imaging volume to display the sensitivity of the array. The standard deviation of the sensitivity was calculated between all scan locations within the imaging volume. Each row of the crosstalk matrix was reshaped to the dimensions of the imaging volume to display the aliasing map of each voxel within the volume.

2.2.6 Performance Metrics

Please refer to section 1.6.2 for signal fidelity measures (mean absolute error and structural similarity index).

The identity matrix and phantom data were once again compared to the crosstalk matrix and image reconstruction, respectively.

2.3 Results

2.3.1 Crosstalk matrix

The sensitivity of the system as well as the aliasing of a voxel in the centre and on the edge of the imaging volume are displayed in Figure 2.3, from left to right, respectively. The uniformity of the sensitivity as well as the total aliasing decreased with increasing directional points and spacing. However, the total sensitivity of the system and the aliasing normalized to the signal in its respective voxel decreased significantly with the same parameters. Sensitivity near the boundary of the imaging volume increased as a result of the implementation of directional points; sensitivity near the centre of the volume of interest decreased.

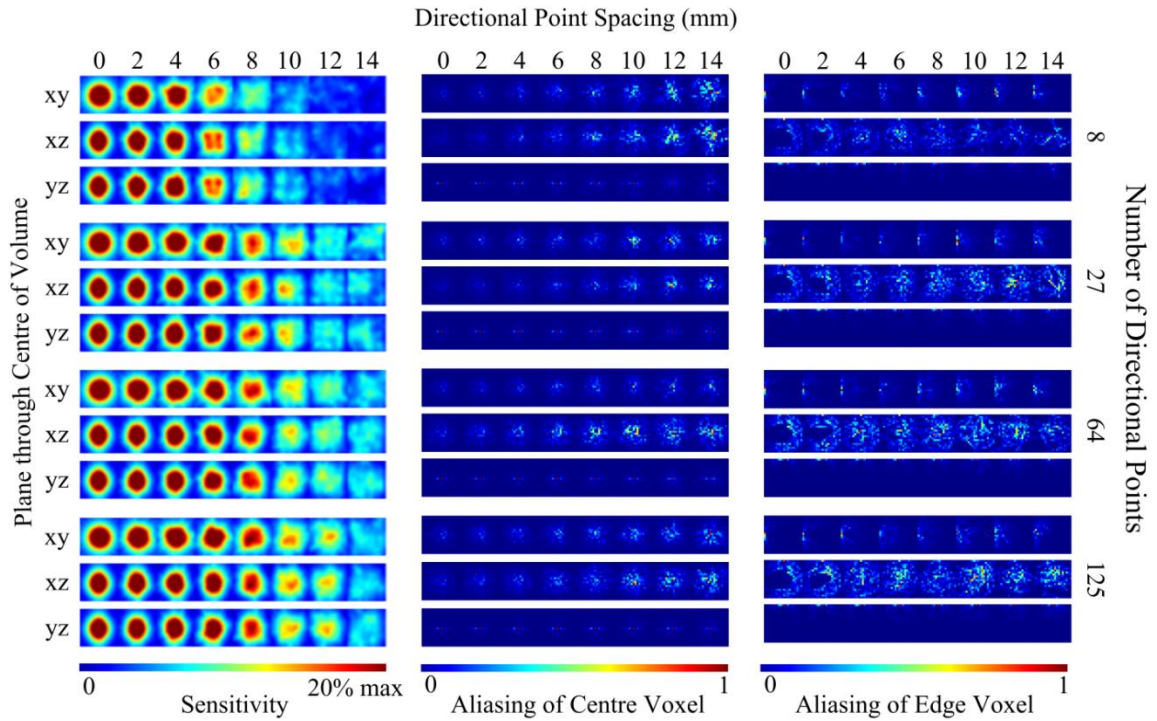


Figure 2.3: Intensity maps indicating the (left to right) sensitivity, aliasing of the centre voxel and aliasing of an edge voxel of the photoacoustic imaging system due to variation of transducer directions within the array. The xy, xz and yz planes through the centre of the volume are shown in the top, middle and bottom of each set of three intensity maps, respectively. The spacing of the directional points in the array was 0 to 14 mm, from left to right along each row of intensity maps. The number of directional points increases from 8 to 125 from the top to bottom for each grouping of three intensity maps.

The mean absolute error and structural similarity between the crosstalk matrix and identity matrix were calculated as a function of cube layers to identify changes in the centre and edges of the volume (Figure 2.4). Each layer is a hollow cube with 1 mm wall thickness and the centre cube is 2 x 2 x 2 mm.

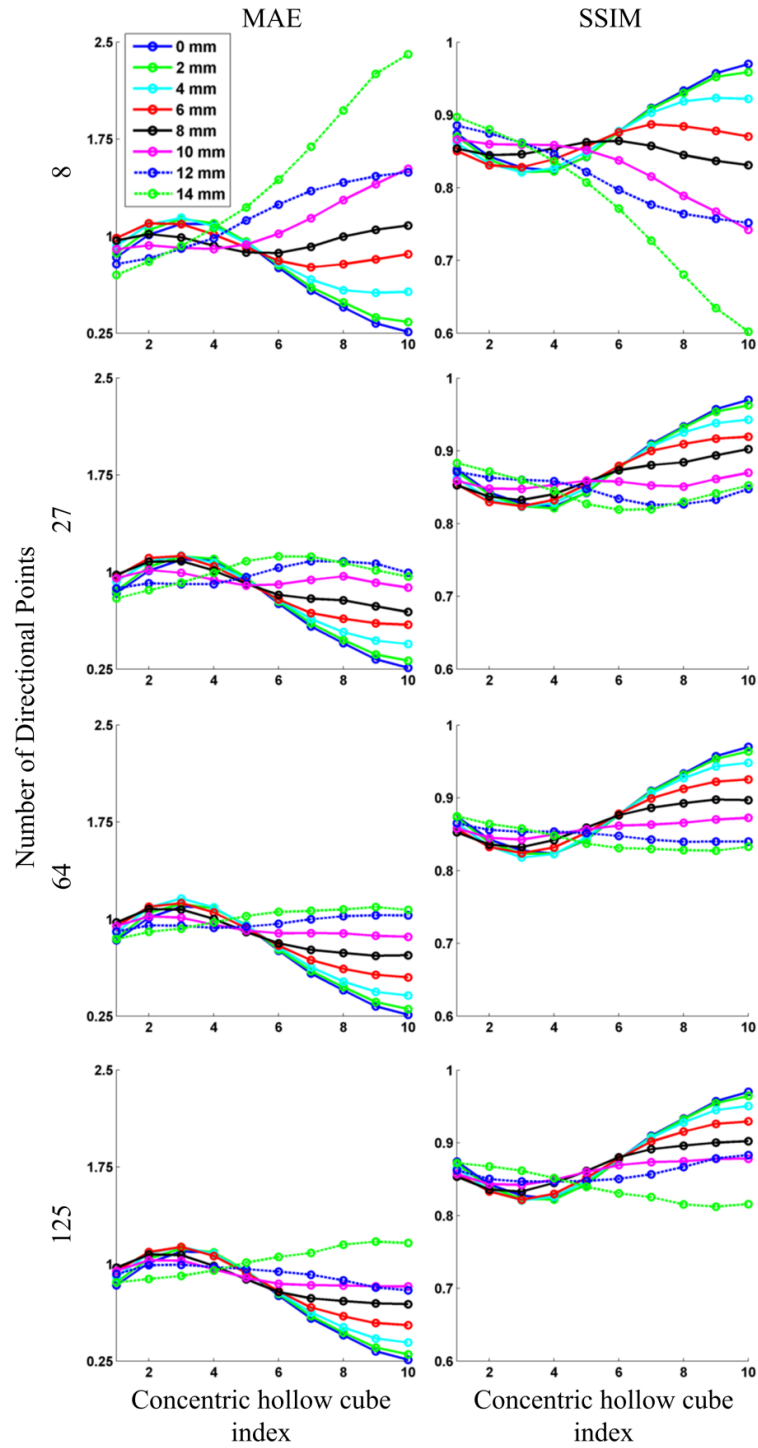


Figure 2.4: Mean absolute error and structural similarity index are shown in the left and right columns, respectively. The number of directional points increases from the top to bottom graph and the spacing of the directional points is indicated in the legend in the top left graph, from 0 mm to 14 mm. The concentric hollow cube index indicates a 1 mm thick cube within the imaging volume from the outside (index 1) to inside (index 10) of the volume.

The MAE was improved for the outer 5 mm of the imaging volume for some cube sizes at all numbers of directional points. All transducers directed towards the centre of the array yielded the lowest MAE for all configurations of focal points within 6 mm of the centre of the array. The SSIM index was highest in the centre 4 or 5 mm of the imaging volume when all transducers were directed towards the centre. The periphery of the imaging volume achieved a better SSIM index with larger directional point spacing.

The MAE and SSIM are shown as intensity maps in Figure 2.5. The lowest MAE values take a spherical shape at the centre of the imaging volume for smaller directional point spacing sizes. The MAE becomes more evenly distributed throughout the volume with increasing spacing size. The system overall has higher MAE values at the top of the volume than the bottom. For 8 directional points, the MAE becomes much higher in the centre of the volume although for greater numbers of directional points this feature is not as prominent. The SSIM index becomes more uniform with increasing directional point spacing but remains relatively low compared to the central-directed case. There is improvement of the SSIM index from 8 directional points to a higher number of points. Qualitative differences between 27, 64 and 125 directional points are less notable between matching directional point spacing. There is noticeable decline in image quality as indicated by the SSIM index between 12 and 14 mm spacings.

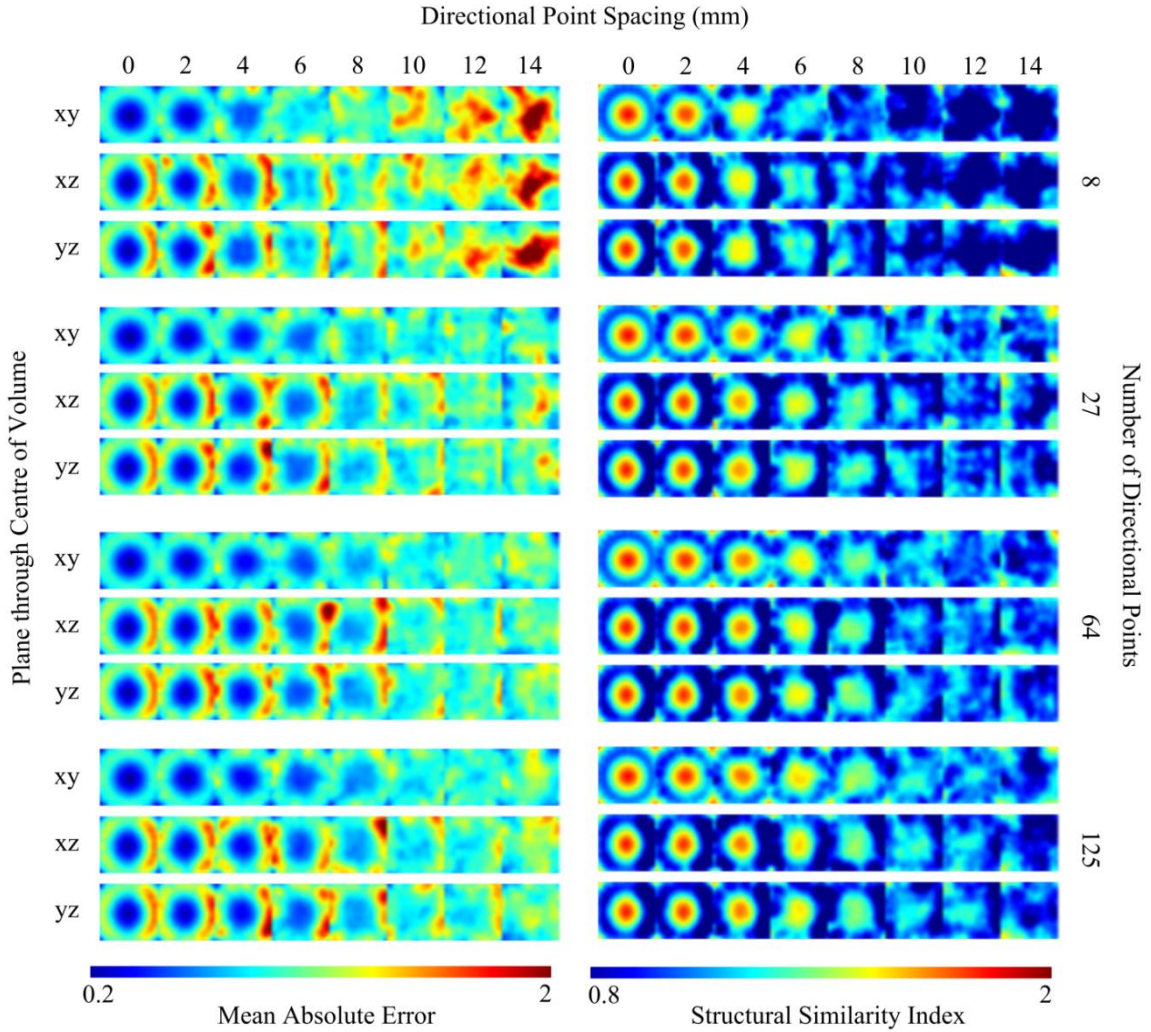


Figure 2.5: Mean absolute error and structural similarity index are shown in the left and right columns, respectively, as intensity maps. The xy, xz and yz planes through the centre of the volume are shown in the top, middle and bottom of each set of three intensity maps, respectively. The spacing of the directional points in the array was 0 to 14 mm, from left to right along each row of intensity maps. The number of directional points increases from 8 to 125 from the top to bottom for each grouping of three intensity maps.

2.3.2 Imaging task

Simulated imaging phantoms reconstructed with the respective pseudoinverse for each number and spacing of directional points are shown in Figure 2.6. The phantom is shown above the imaging results. The MAE and SSIM index are shown in Figure 2.7 as a function of number and spacing of directional points. For the grid of points, the overall MAE decreased with increased directional point spacing with the exception of 8 directional points which reaches a minimum MAE at a spacing of 8 mm and increases

dramatically for higher spacing dimensions. The lowest MAE was accomplished with 64 directional points spaced on a 14 mm cube. The SSIM index increased with increasing cube size, excluding 8 directional points which began to decrease after the 8 mm cube spacing. The highest SSIM index measure was achieved with 64 directional points spaced on a 14 mm cube.

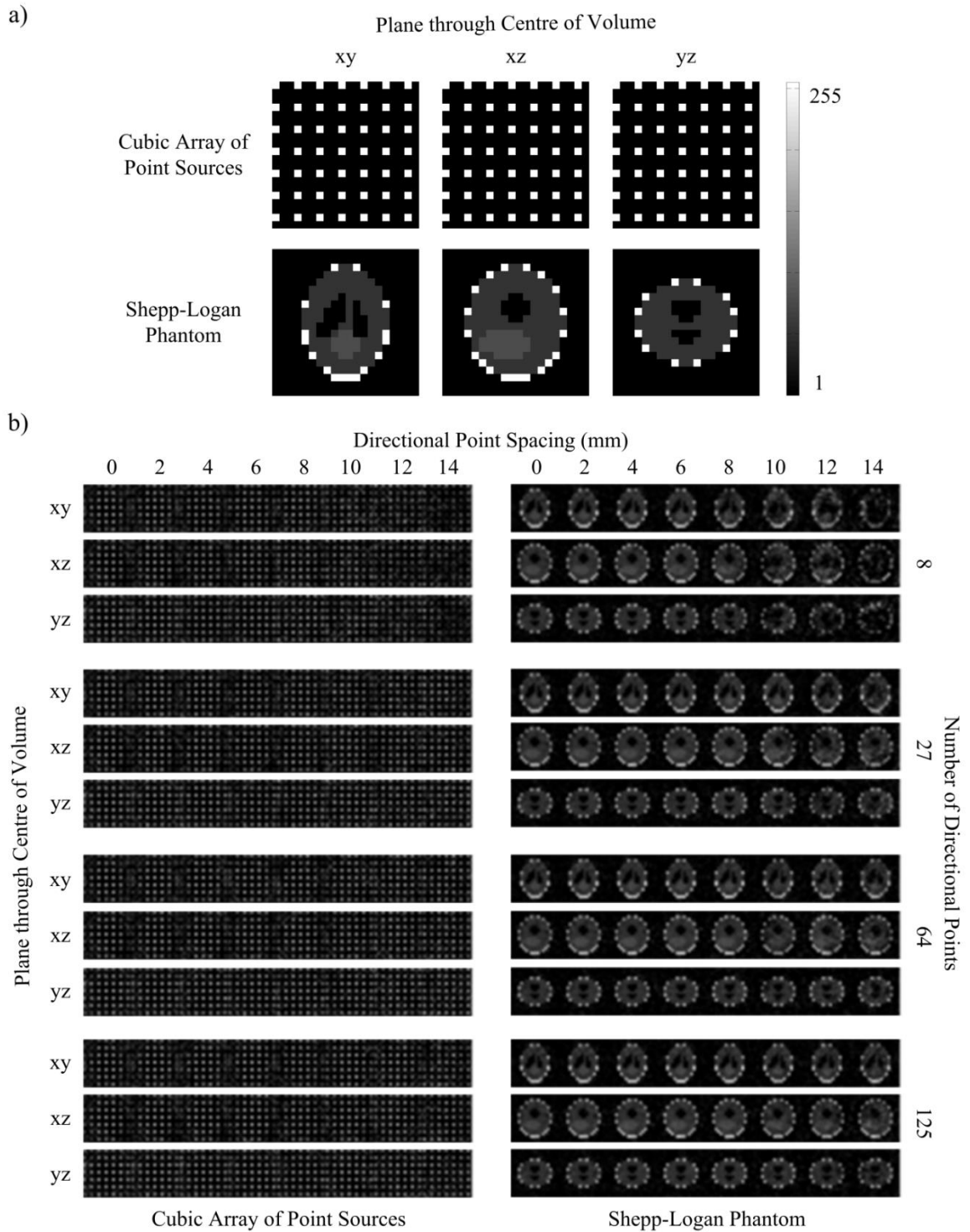


Figure 2.6: (a) The xy, xz and yz planes through the centre of the imaging phantoms. The scale bar applies to all images. (b) Reconstructed images utilizing increasing spacing of directional points (left to right) and number of directional points (top to bottom) within the transducer array are shown for the array of point sources (centre) and Shepp-Logan phantom (right).

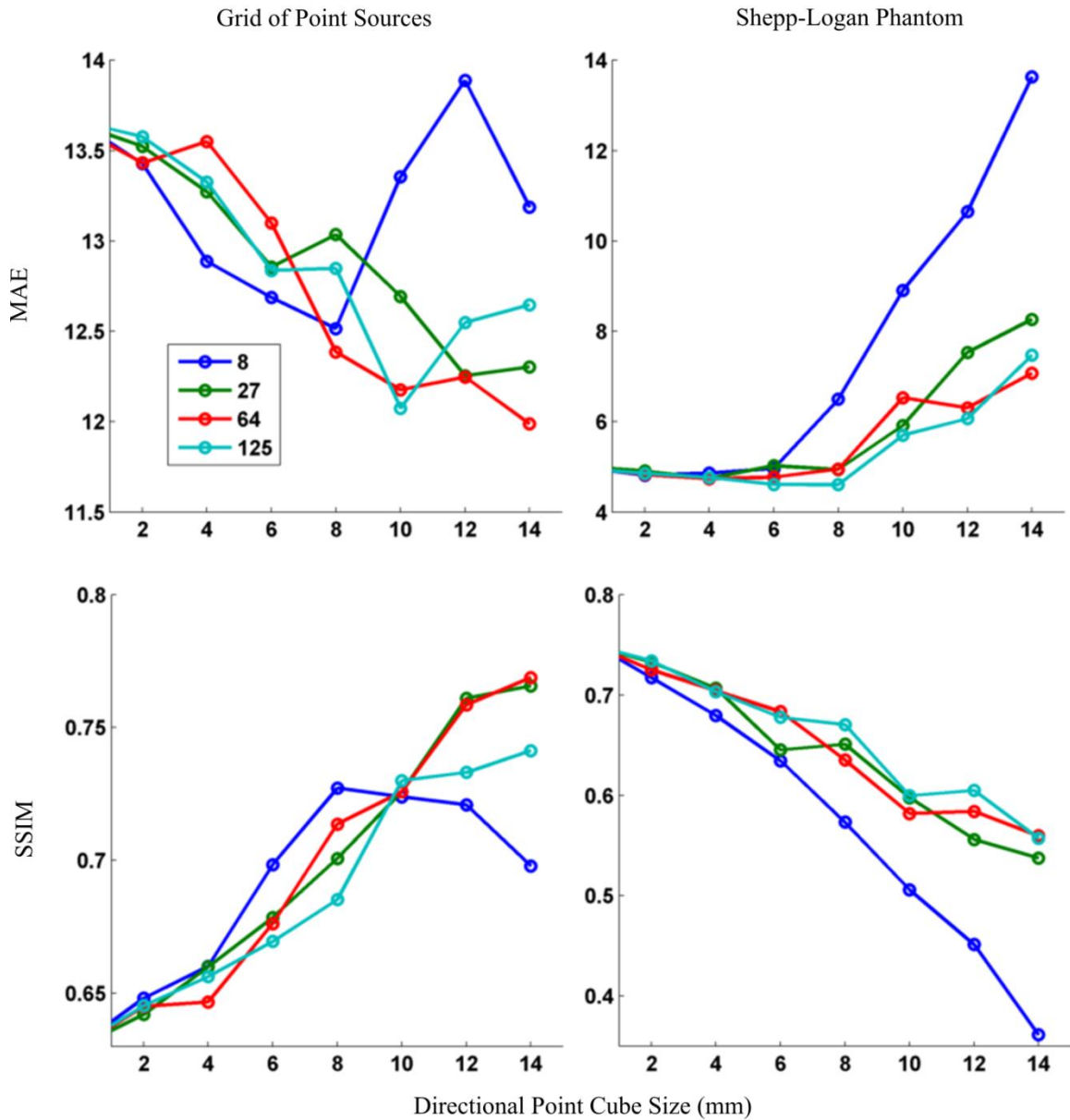


Figure 2.7: Mean absolute error (top) and structural similarity index (bottom) for the phantom imaging tasks are shown for the array of point sources (left) and Shepp-Logan phantoms (right).

The Shepp-Logan phantom imaging results gave dissimilar performance metrics to the grid phantom. The MAE is nearly identical for spacings up to 8 mm for larger numbers of directional points but then increases significantly for larger spacings. The SSIM index measures decreased with increasing spacing for all numbers of directional points, 8 directional points causing the greatest decrease. The highest 3D-SSIM was achieved with all transducers directed towards the centre of the array.

2.4 Discussion

2.4.1 Crosstalk matrix

We have successfully modeled a photoacoustic imaging system with similar properties to our own and modified the directionality of the transducers within it. The sensitivity maps taken from the crosstalk matrix of the system showed increasing uniformity within the imaging volume but decreased sensitivity overall. With all transducers directed towards the centre of the array, the sensitivity in the centre greatly outweighed the sensitivity in the periphery of the volume. When transducers were directed elsewhere, the increase in sensitivity in the outskirts of the region was less than that lost at the centre and resulted in an overall decreased sensitivity of the system. The increased loss at the centre of the volume when utilizing 8 directional points at larger cube spacings was expected as the transducers were directed towards the corners of the volume, limiting their angular acceptance and restricting signal from the centre of the volume. This drastic of a decrease in signal was not present for larger numbers of directional points as spacing more points meant some transducers were directed close to or in the centre of the volume.

Aliasing in the centre voxel increased with increasing directional point spacing in the aliasing maps. This can be seen particularly in the case of eight directional points. Because the aliasing map is normalized to the sensitivity, the ratio of signal to aliasing increases substantially while the overall aliasing decreases for increasing directional point spacing. Aliasing for 27, 64 and 125 directional points increased less than eight points within the intensity maps, although this can partially be attributed to the sensitivity of the centre voxel not decreasing as significantly.

Analysis of the crosstalk matrix takes both the sensitivity and aliasing of the system into account. Calculating the MAE between the crosstalk and identity matrix means that high, uniform sensitivity and minimal aliasing within the crosstalk would result in the lowest MAE values. The MAE was most variable in the centre of the volume as there was the greatest change in coverage from transducers within this volume. It was expected that the case with all transducers directed towards the centre would outperform other parameters in the core of the volume as all transducers in this case can detect signal

from the centre of the volume. When transducers were directed at points further from the centre, the drop in signal amplitude resulted in lower detection. All transducers directed towards the centre remained the ideal case for the innermost 10x10x10 mm cube of the volume over all other combinations of directional points. The outer portions of the imaging volume, namely between the seventh and ninth concentric hollow cube (cube index 2 – 4, Figure 2.4), performed better than the case with all transducers directed at the centre. In the outermost concentric hollow cube, 10 mm away from the centre of the volume, all transducers directed at the centre was the worst or nearly worst performing parameter. Because all of the detection was focused at the centre of the volume, the outskirts had up to 30 times less signal detection than at the centre. Changing the forward facing direction of the transducers away from the centre improved the MAE slightly for larger cube spacings of the directional points by increasing sampling of the outskirts of the cube. However, the increased angle and distance from the transducer face to the volume also caused sampling outside of the region of interest. This wasted useful information and resulted in decreased overall sensitivity, particularly in the centre of the volume.

In general, the SSIM index and MAE metrics displayed similar trends. All transducers directed toward the centre of the imaging volume was optimal for the centre of the volume and was less desirable when the cube spacing reached sizes larger than 8 – 10 mm. The SSIM index was higher for large spacings of directional points in the outskirts of the imaging volume, yet these same spacings greatly underperform in the centre. Although SSIM takes into account spatial distortions, the crosstalk matrix does not have complex anatomical features to be distinguished and it was expected to give similar results to MAE.

2.4.2 Imaging task

Reconstructions based on the imaging operator were acquired for the point sources as well as the Shepp-Logan phantom. Both MAE and SSIM indicated decreased image quality with the utilization of directional points based on crosstalk matrix analysis, yet the point source imaging task benefitted from directional point use. Imaging results from the Shepp-Logan phantom were consistent with the findings from the crosstalk

matrix analysis. This was likely due to the nature of the object of interest. The slightly increased sensitivity of the system to signals in the periphery of the volume allowed for improved detection of points in the outskirts of the region and the decrease at the centre was not significantly detrimental in resolving the points at the core. Conversely, the Shepp-Logan imaging task did not contain a large proportion of the object in the outskirts of the volume. Resolving details in the centre of the image was hindered by directing transducers away from the region. These results can be most effectively utilized by optimizing transducer arrays for the specific targets being imaged. Spherical targets are more effectively imaged with centrally directed transducers, while varying directional points can be used to assess cuboid targets with features located throughout the volume.

2.4.3 Implementation and Considerations

Other studies concerning how to increase the sampling within an imaging volume have been performed by investigating the number of transducers [29], translating transducers around the volume [30] and increasing the angular acceptance and sensitivity of the transducers in the array [31]. This is the first study exploring a staring hemispherical transducer array for photoacoustic imaging that investigates the directionality of transducers. Setting a number of points to direct transducers towards can be compared to splitting the 129 transducer array into multiple, more sparsely populated arrays or translating less populated arrays around each point in the imaging volume. Utilizing stationary transducers in this case is disadvantageous to the sensitivity of the system as the distance to each point is larger than for a smaller scanning array.

The simulated transducer array is a fairly good representation of the physical system, however the transducers are built in-house and are not identical in their response. This model conservatively used a transducer with an angular response in the lower range. The transducer array will, in practice, contain transducers with varying angular and frequency responses which will lead to some inhomogeneity compared to the simulated case. Due to the conservative angular acceptance of the simulated array, it is expected that the physical array would slightly outperform its virtual counterpart.

2.5 Conclusion

An existing photoacoustic imaging system was characterized and a simulated model developed to vary the directionality of transducers within it. Between 8 and 125 directional points were evenly placed on a cube and roughly equal numbers of transducers were directed towards each one. System performance was determined by analysing the crosstalk matrix of the system as well as performing an imaging task based on the experimentally obtained imaging operator. Mean absolute error and structural similarity were calculated for each combination of system directionality parameters. Altering the directionality of transducers lead to higher signal fidelity for imaging targets spaced throughout the entire imaging volume but did not improve imaging for spherical targets located in the centre of the region of interest.

2.6 References

- [1] M. Xu and L. V. Wang, "Photoacoustic imaging in biomedicine," *Rev. Sci. Instrum.*, vol. 77, no. 4, p. 041101, 2006.
- [2] C. Li and L. V. Wang, "Photoacoustic tomography and sensing in biomedicine.," *Phys. Med. Biol.*, vol. 54, no. 19, pp. R59–97, Oct. 2009.
- [3] R. Ma, M. Distel, X. L. Deán-Ben, V. Ntziachristos, and D. Razansky, "Non-invasive whole-body imaging of adult zebrafish with optoacoustic tomography.," *Phys. Med. Biol.*, vol. 57, no. 22, pp. 7227–37, Nov. 2012.
- [4] J. Xia, M. Chatni, K. Maslov, and L. V. Wang, "Anatomical and metabolic small-animal whole-body imaging using ring-shaped confocal photoacoustic computed tomography," *Proc. SPIE*, vol. 8581, p. 85810K–85810K–6, Mar. 2013.
- [5] L. Xi, S. R. Grobmyer, L. Wu, R. Chen, G. Zhou, L. G. Gutwein, J. Sun, W. Liao, Q. Zhou, H. Xie, and H. Jiang, "Evaluation of breast tumor margins in vivo with intraoperative photoacoustic imaging.," *Opt. Express*, vol. 20, no. 8, pp. 8726–31, Apr. 2012.
- [6] R. A. Kruger, R. B. Lam, D. R. Reinecke, S. P. Del Rio, and R. P. Doyle, "Photoacoustic angiography of the breast," *Med. Phys.*, vol. 37, no. 11, 2010.
- [7] K. S. Valluru, B. K. Chinni, N. a. Rao, S. Bhatt, and V. S. Dogra, "Development of a c-scan photoacoustic imaging probe for prostate cancer detection," vol. 7968, p. 79680C–79680C–7, Mar. 2011.
- [8] R. Bitton, R. Zemp, J. Yen, L. V. Wang, and K. K. Shung, "A 3-D high-frequency array based 16 channel photoacoustic microscopy system for in vivo micro-vascular imaging.," *IEEE Trans. Med. Imaging*, vol. 28, no. 8, pp. 1190–7, Aug. 2009.
- [9] R. Bitton, R. Zemp, J. Yen, L. H. Wang, and K. K. Shung, "Design of a high frequency array based photoacoustic microscopy system for micro-vascular imaging.," *Conf. Proc. IEEE Eng. Med. Biol. Soc.*, vol. 2007, pp. 2175–8, Jan. 2007.
- [10] L. V. Wang, "Multiscale photoacoustic microscopy and computed tomography.," *Nat. Photonics*, vol. 3, no. 9, pp. 503–509, Aug. 2009.
- [11] P. Beard, "Biomedical photoacoustic imaging.," *Interface Focus*, vol. 1, no. 4, pp. 602–31, Aug. 2011.

- [12] B. Wang, L. Xiang, M. S. Jiang, J. Yang, Q. Zhang, P. R. Carney, and H. Jiang, "Photoacoustic tomography system for noninvasive real-time three-dimensional imaging of epilepsy.," *Biomed. Opt. Express*, vol. 3, no. 6, pp. 1427–32, Jun. 2012.
- [13] M. B. Roumeliotis, "Real-Time Three-Dimensional Photoacoustic Imaging," University of Western Ontario, 2011.
- [14] J. Gamelin, D. Castillo, L. V Wang, A. Aguirre, A. Maurudis, F. Huang, and Q. Zhu, "Curved array photoacoustic tomographic system for small animal imaging.," *J. Biomed. Opt.*, vol. 13, no. 2, p. 024007, 2013.
- [15] D. Yang, L. Zeng, C. Pan, X. Zhao, and X. Ji, "Noninvasive photoacoustic detecting intraocular foreign bodies with an annular transducer array.," *Opt. Express*, vol. 21, no. 1, pp. 984–91, Jan. 2013.
- [16] J. Gamelin, A. Maurudis, A. Aguirre, F. Huang, P. Guo, L. V Wang, and Q. Zhu, "A real-time photoacoustic tomography system for small animals.," *Opt. Express*, vol. 17, no. 13, pp. 10489–98, Jun. 2009.
- [17] L. Xi, X. Li, L. Yao, S. Grobmyer, and H. Jiang, "Design and evaluation of a hybrid photoacoustic tomography and diffuse optical tomography system for breast cancer detection.," *Med. Phys.*, vol. 39, no. 5, pp. 2584–94, May 2012.
- [18] P. Ephrat, L. Keenliside, A. Seabrook, F. S. Prato, and J. J. L. Carson, "Three-dimensional photoacoustic imaging by sparse-array detection and iterative image reconstruction.," *J. Biomed. Opt.*, vol. 13, no. 5, p. 054052, 2010.
- [19] M. Roumeliotis, R. Z. Stodilka, M. a Anastasio, G. Chaudhary, H. Al-Abed, E. Ng, A. Immucci, and J. J. L. Carson, "Analysis of a photoacoustic imaging system by the crosstalk matrix and singular value decomposition.," *Opt. Express*, vol. 18, no. 11, pp. 11406–17, May 2010.
- [20] M. P. Fronheiser, S. a Ermilov, H.-P. Brecht, A. Conjusteau, R. Su, K. Mehta, and A. a Oraevsky, "Real-time optoacoustic monitoring and three-dimensional mapping of a human arm vasculature.," *J. Biomed. Opt.*, vol. 15, no. 2, p. 021305, 2014.
- [21] S. A. Ermilov, H.-P. Brecht, M. P. Fronheiser, V. Nadvoretzky, R. Su, A. Conjusteau, and A. a Oraevsky, "In vivo 3D visualization of peripheral circulatory system using linear optoacoustic array," *Proc. SPIE*, vol. 7564, no. 713, pp. 756422–756422–8, Feb. 2010.
- [22] I. Kosik and J. J. L. Carson, "Real-time multispectral 3-D photoacoustic imaging of blood phantoms," *Proc. SPIE*, vol. 8581, p. 85811V, Mar. 2013.

- [23] M. Roumeliotis, P. Ephrat, J. Patrick, and J. J. L. Carson, "Development and characterization of an omni-directional photoacoustic point source for calibration of a staring 3D photoacoustic imaging system," *Opt. Express*, vol. 17, no. 17, p. 15228, Aug. 2009.
- [24] M. Roumeliotis, R. Z. Stodilka, M. a Anastasio, E. Ng, and J. J. L. Carson, "Singular value decomposition analysis of a photoacoustic imaging system and 3D imaging at 0.7 FPS.," *Opt. Express*, vol. 19, no. 14, pp. 13405–17, Jul. 2011.
- [25] M. Schabel, "3D Shepp-Logan phantom," *MATLAB Central File Exchange*, 2006. [Online]. Available: <http://www.mathworks.com/matlabcentral/fileexchange/9416-3d-shepp-logan-phantom>. [Accessed: 20-Nov-2013].
- [26] M. P. Holmes, A. G. Gray, C. L. Isbell, and G. Tech, "QUIC-SVD : Fast SVD Using Cosine Trees," pp. 1–8.
- [27] Z. Wang, A. C. Bovik, H. R. Sheikh, E. P. Simoncelli, and S. S. Member, "Image quality assessment: from error visibility to structural similarity.," *IEEE Trans. Image Process.*, vol. 13, no. 4, pp. 600–12, Apr. 2004.
- [28] P. Wong, "Three-dimensional Photoacoustic Tomography System Design Analysis and Improvement," The University of Western Ontario, 2014.
- [29] A. Dima, N. C. Burton, and V. Ntziachristos, "Multispectral optoacoustic tomography at 64, 128, and 256 channels.," *J. Biomed. Opt.*, vol. 19, no. 3, p. 36021, Mar. 2014.
- [30] R. a Kruger, C. M. Kuzmiak, R. B. Lam, D. R. Reinecke, S. P. Del Rio, and D. Steed, "Dedicated 3D photoacoustic breast imaging.," *Med. Phys.*, vol. 40, no. 11, p. 113301, Nov. 2013.
- [31] W. Xia, D. Piras, J. C. G. van Hespén, S. van Veldhoven, C. Prins, T. G. van Leeuwen, W. Steenbergen, and S. Manohar, "An optimized ultrasound detector for photoacoustic breast tomography.," *Med. Phys.*, vol. 40, no. 3, p. 032901, Mar. 2013.

Chapter 3

3 Implementation of a shaped matching layer as an acoustic lens for transducers in a staring transducer array for photoacoustic imaging

This chapter is based on a manuscript currently being prepared for publication in a peer-reviewed journal. The work presented in this chapter aimed to increase the field of view of a photoacoustic imaging system by increasing the angular acceptance of transducers using a shaped matching layer.

3.1 Introduction

3.1.1 Background

Photoacoustic tomography (PAT) acquires images by detecting ultrasound waves generated from tissues after the absorption of energy supplied by a laser pulse. The bipolar pressure waves produced by the thermoelastic expansion are detected by transducers positioned around the absorber and used to reconstruct approximations of the absorbers. The modality is non-invasive, non-ionizing and makes use of endogenous chromophores for contrast [1][2]. Photoacoustic tomography offers improved penetration depth and resolution over optical imaging and has been applied to various imaging tasks including whole-body small animal imaging [3][4], breast imaging [5][6], prostate imaging [7], characterization of vasculature [8] and microscopy [9][10].

3.1.2 Photoacoustic transducer limitations

Due to the limited penetration depth of light, the transducers used in biomedical PAT are required to detect weak signals originating from up to several centimeters within tissue. For high sensitivity, large transducer elements outperform their smaller area counterparts. However, angular acceptance is greater for small-area transducers. Small angular acceptance results in a limited field of view (FOV) and reduced lateral resolution of a PAT system [11]. In order to increase the angular acceptance of a large diameter transducer, Pramanik et al. proposed the use of an acrylic negative acoustic lens [12]. Acoustic lenses follow Snell's law and by using appropriate materials are able to direct photoacoustic signals, otherwise lost, toward the transducer element. Since this initial

work acoustic lenses have been investigated through simulation and experimentation and have been utilized in photoacoustic microscopy and breast imaging [13][14][15].

3.1.3 Acoustic lens material

The ideal acoustic lens material should provide adequate refraction to cause lensing but with minimal insertion loss. Thus, the lens should have a speed of sound greater than the coupling medium, minimal acoustic attenuation, and acoustic impedance as similar to the coupling medium or tissue as possible. To date, plastics and resins such as acrylic and PMMA have been cut or molded for use as acoustic lenses [12][15]. Xia et al. noted that the acoustic lens acts as a second impedance matching layer between the transducer element and coupling medium and it was proposed that multiple matching layers could be utilized to minimize reflection loss [15]. We propose that a single, shaped matching layer can alternatively be used as an acoustic lens.

3.1.4 Objective and Approach

The objective of this work was to increase the field of view of a staring transducer array for photoacoustic imaging by increasing the angular acceptance of individual transducers. This was achieved by applying a shaped matching layer to the face of transducers which acted as an acoustic lens and aided in directing pressure waves toward the transducer element. Individual transducer angular acceptance was measured in the absence of a matching layer, with a flat epoxy matching layer, and with a convex epoxy matching layer to address the effects of both adding a matching layer and changing its shape. Transducer response data was fit and the representative equation was used in a simulated model of a 129 channel staring transducer array. The sensitivity, aliasing, mean absolute error (MAE) and structural similarity (SSIM) index of the transducer array for each matching layer case were found to assess the effect on a PAT system. A simulated imaging task was performed using a cubic array of points and a Shepp-Logan phantom and both were assessed with MAE and SSIM index to determine repercussions of the matching layer on image quality.

3.2 Methods

3.2.1 Transducer matching layer and characterization

Four 2.7 MHz transducers (~124% bandwidth) built in-house were characterized with no matching layer, flat, and convex epoxy matching layers. Speed Set™ epoxy (LePage, Mississauga, Ontario) was applied to the transducer face by hand within three minutes of mixing the resin and hardener epoxy components. Transducers were immobilized with the transducer axis perpendicular to the ground to evenly distribute epoxy on the surface. To achieve a flat epoxy matching layer, epoxy was applied to the face of the transducer until the epoxy level was flush with the casing of the transducer. For a convex epoxy matching layer, epoxy was applied to the face of the transducer until a hemispherical shape was achieved due to the surface tension of the epoxy. The physical shape of each transducer face with and without matching layers was quantified by performing a 3D scan (NextEngine, California). Representative scans for each case can be seen in Figure 3.1. The depression between the transducer face and casing without epoxy was measured to be $0.57 \text{ mm} \pm 0.04 \text{ mm}$ and the height of the convex epoxy from the casing to its highest point was $1.81 \text{ mm} \pm 0.16 \text{ mm}$ between the four transducers.

The angular acceptance and response of each transducer was measured by scanning a photoacoustic point source affixed to a SCARA robot (Model E2C351A – UL, Epson) along a semicircular path with the transducer to be characterized located at the centre. The point source was 3 cm away from the centre of the transducer face and scanned through 170 degrees at two degree increments, totalling 85 locations on the semicircle. Another transducer was mounted on the robotic arm in order to maintain a fixed distance and orientation between the point source and transducer. Six signals from three independent trials were collected for each position along the semicircular path and for each matching layer case. Signals were corrected for inhomogeneity of the point source emission profile (please refer to section 2.2.1 for point source construction and characterization) as well as any laser output inhomogeneity by normalizing to the signal detected by the transducer.

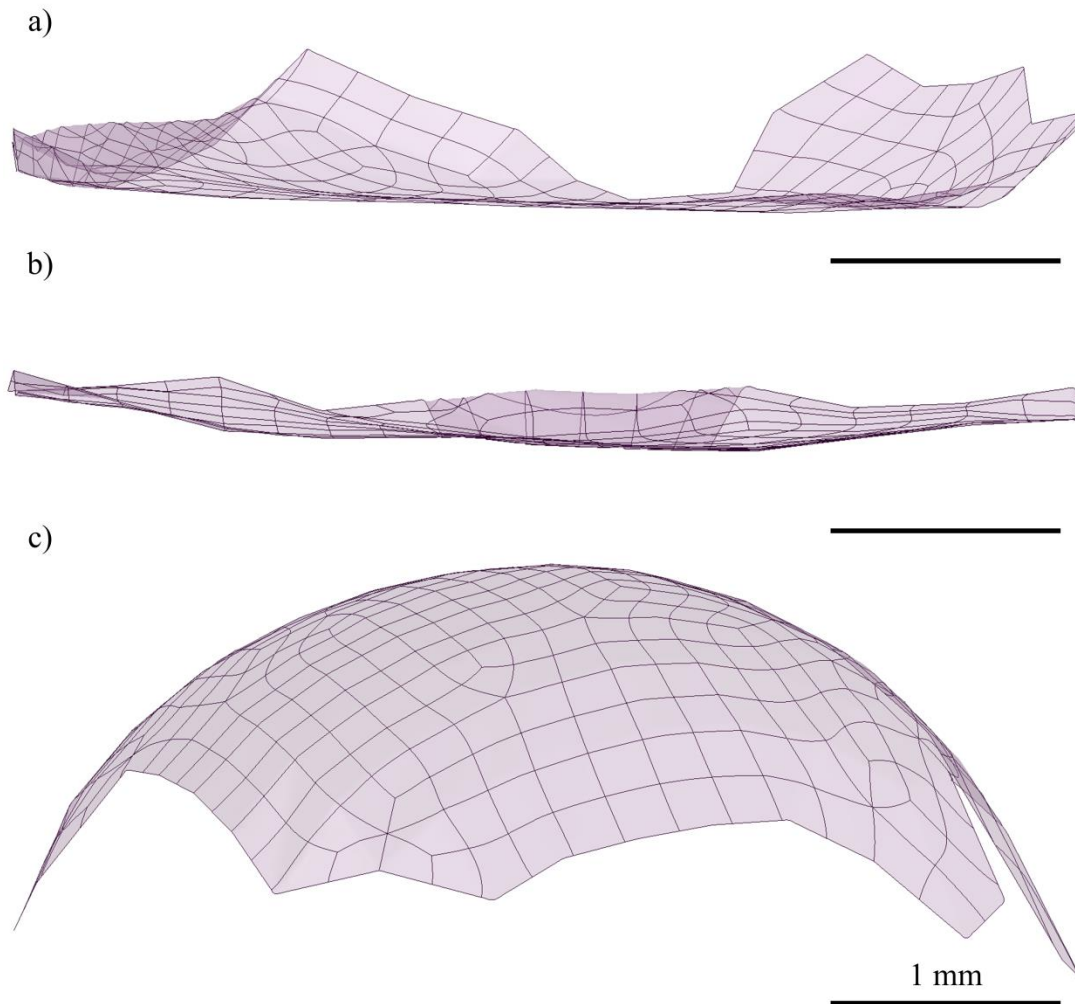


Figure 3.1: The cross-section of a 3D representation of the transducer face, where (a) has no matching layer, (b) has a flat epoxy matching layer and (c) has a convex epoxy matching layer. The scale bar represents 1 mm in all cases and the transducer element is approximately 5 mm in diameter.

The signal intensity measurements from three trials for each of four transducers were averaged for each matching layer case and plotted as a function of the angle away from normal to the transducer face. Each data set was fit with an empirical equation (Figure 3.2). In all cases the R^2 value for the fit to the data was greater than 0.999.

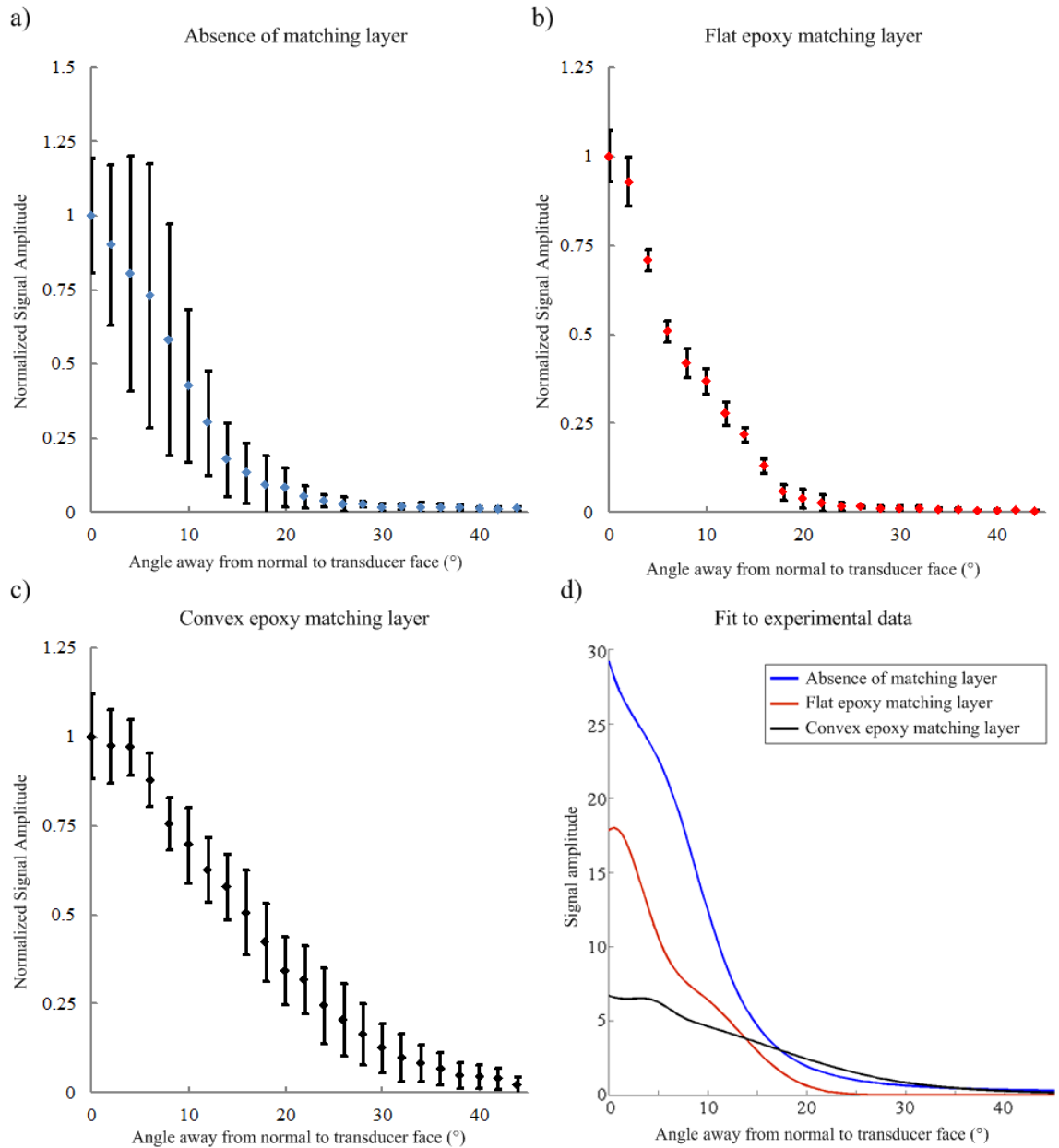


Figure 3.2: Normalized signal amplitude of the transducers as a function of angle away from normal to the transducer face with (a) no matching layer, (b) a flat matching layer and (c) a convex matching layer. The empirically determined equations fit to (a), (b) and (c) are shown in (d). (d) Fitted equations to transducer response with no matching layer (blue line), a flat matching layer (red line) and a convex matching layer (black line).

3.2.2 Modelling of Photoacoustic Imaging System

A 128 channel photoacoustic staring transducer array was modeled in Matlab which utilized the equation fit to the signal response of transducers without a matching layer, or with a flat or convex epoxy matching layer. Transducer locations are shown as a point cloud in Figure 3.3 (a). The sensitivity of the arrays populated with transducers from each of the three cases was determined by calculating the crosstalk matrix of the system, as described in section 1.6.1 [16]. The representative photoacoustic point source signal used is shown in Figure 3.3 (b). This response of the array to each voxel within the volume is known as the imaging operator.

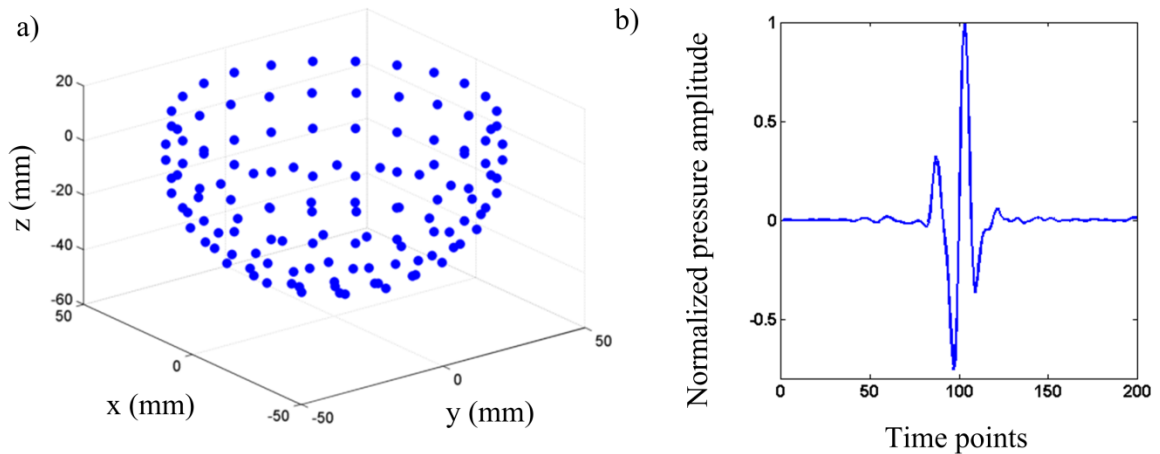


Figure 3.3: Parameters of the simulated photoacoustic imaging system. (a) A point cloud representation of the location of transducers within a hemispherical staring array with a radius of 48 mm. (b) Representative signal attained from averaging 64000 signals from a point-like source.

3.2.3 Evaluation methods

Please refer back to section 1.6.1 for a detailed explanation of the crosstalk matrix.

To quantitatively assess the performance of each matching layer case, the MAE and SSIM index between the crosstalk matrix and the ideal case was found. Details about both MAE and SSIM index can be found in section 1.6.2. An imaging task was performed with a Shepp-Logan phantom to assess the effect of the matching layer shape with imaging performance. Image reconstruction was performed according to section 1.4

and noise added at a signal to noise ratio (SNR) of 10. The MAE and SSIM index were calculated between each case and the original phantom.

3.3 Results

3.3.1 Transducer array simulated response

The sensitivity of the PA transducer array as well as the aliasing of a voxel in the centre and on the edge of the imaging volume are displayed in Figure 3.4, from left to right, respectively. The relative sensitive volume is largest for the case with a convex epoxy matching layer and smallest for the case with the flat epoxy matching layer. However, the absolute value of the sensitivity in the no matching layer case is approximately 3 times higher than for the flat epoxy matching layer and 20 times higher than the convex matching layer case. The aliasing results are comparable between matching layer cases, although because the aliasing is proportional to the signal from the respective voxel (centre or edge), an overall decrease in signal intensity in the convex matching layer case may cause the aliasing to appear stronger.

In order to assess both the sensitivity and aliasing of the system with a quantitative approach, the MAE and SSIM index were measured as a function of cube layers. Each layer is a hollow cube with 1 mm wall thickness with the centre cube corresponding to a 2 x 2 x 2 mm cube. The outermost cube was assigned the cube index of 1 and the innermost layer an index of 10 (Figure 3.5).

The MAE and SSIM index give similar results for the crosstalk matrix analysis. The no matching layer case performed optimally for all regions in the imaging volume except the innermost cube, where the flat matching layer was slightly more desirable. The convex epoxy matching layer was not optimal for any section within the region of interest.

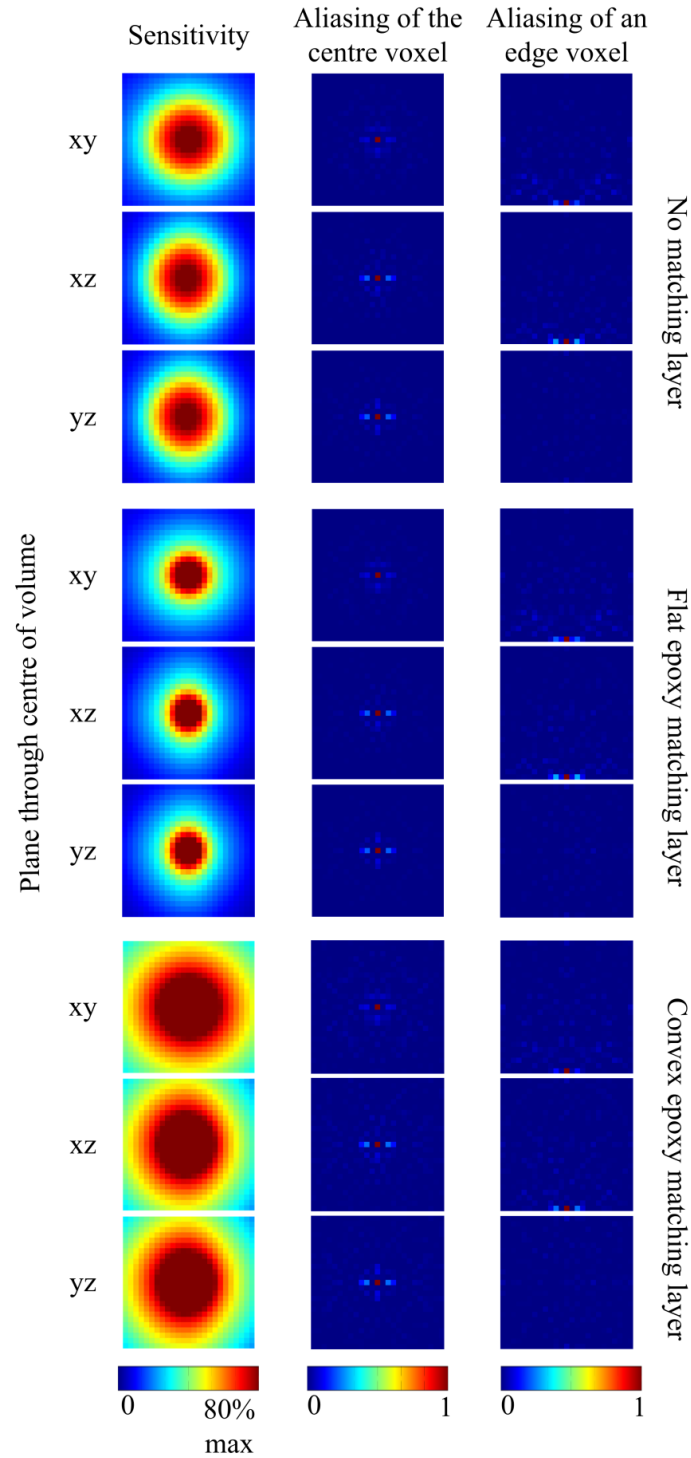


Figure 3.4: Intensity maps indicating the (left to right) sensitivity, aliasing of the centre voxel and aliasing of an edge voxel of the photoacoustic imaging system for three matching layer cases (top to bottom): no matching layer, a flat epoxy matching layer and a convex epoxy matching layer. Sensitivity maps are shown from 0 to 80% of the maximum sensitivity and aliasing maps are normalized to 1, corresponding to

the signal amplitude in the respective voxel. The 25 mm x 25 mm xy, xz and yz planes through the centre of the volume are shown in the top, middle and bottom of each set of three intensity maps, respectively.

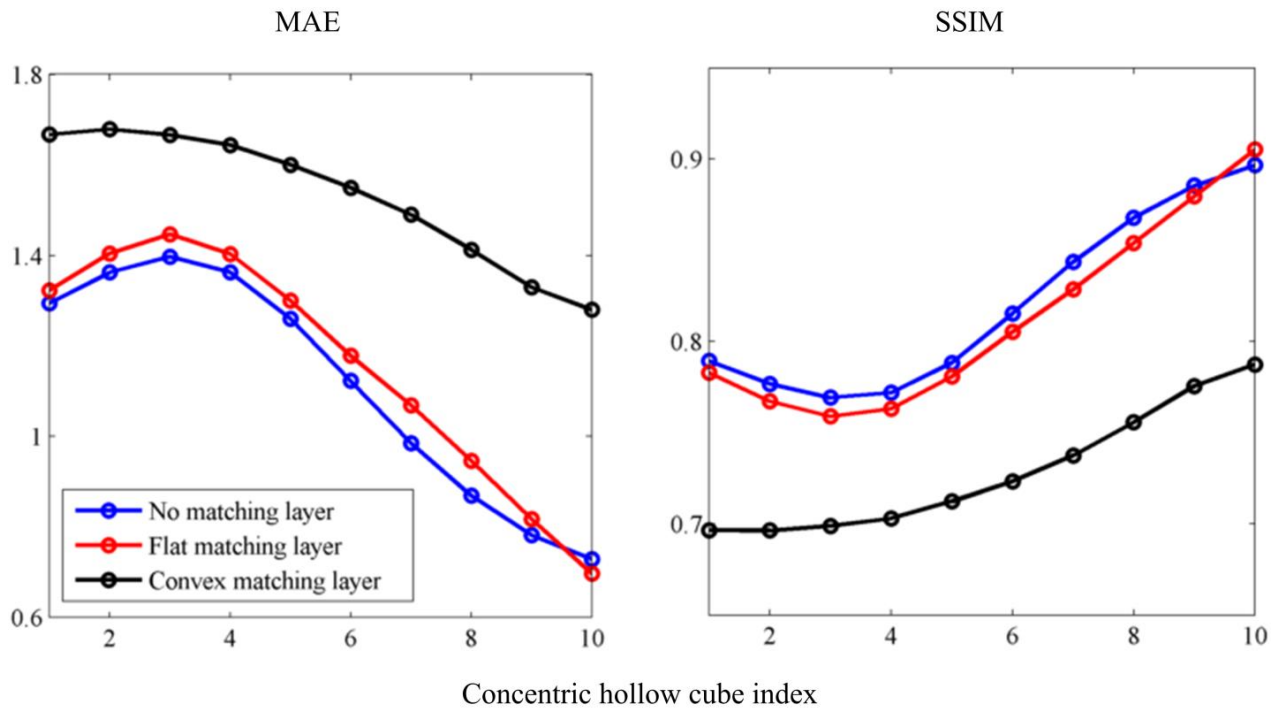


Figure 3.5: Mean absolute error and structural similarity index are shown in the left and right panels, respectively. No matching layer, a flat matching layer and convex matching layer are shown in blue, red and black, respectively. The concentric hollow cube index indicates a 1 mm thick cube within the imaging volume from the outside (concentric hollow cube index 1) to inside (index 10) of the volume.

Simulated image reconstruction of a cubic array of points and a Shepp-Logan phantom using the pseudoinverse from each matching layer case is shown in Figure 3.6. Visually, the results are comparable, with no major distinctions in image quality. For the cubic array of points, the MAE was 3.01, 2.92 and 2.79 for no matching layer, a flat matching layer and a convex matching layer, respectively. The SSIM index was 0.99 for all cases. For reconstruction of the Shepp-Logan phantom, the MAE was 3.32, 3.26 and 2.77 and the SSIM index was 0.63, 0.65 and 0.76 for no matching layer, flat, and convex matching layers, respectively.

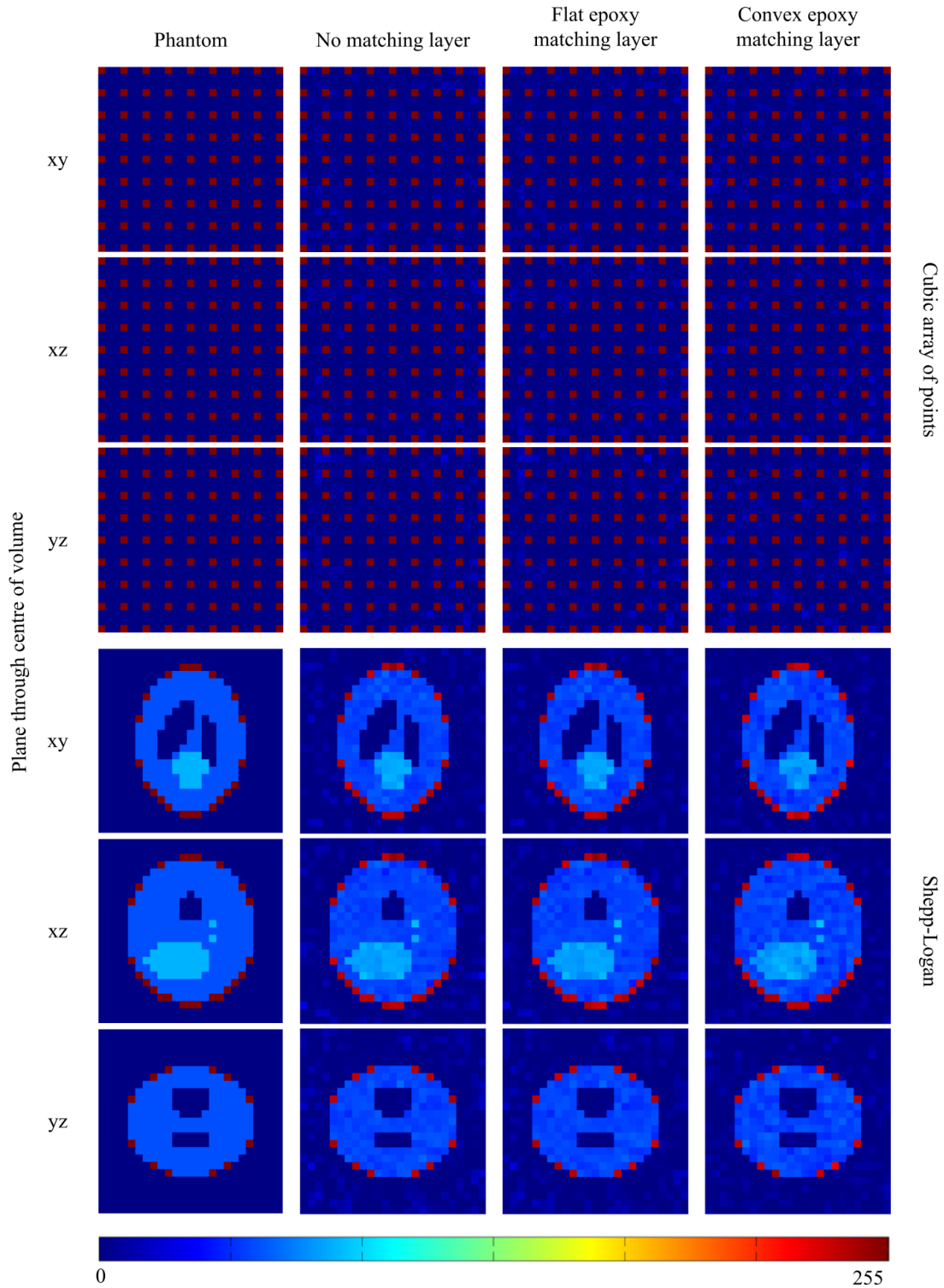


Figure 3.6: Imaging task with a cubic array of points (top) and Shepp-Logan phantom (bottom). The columns show the phantom, no matching layer, flat matching layer and convex matching layer reconstructions from left to right, respectively. The 25 x 25 mm xy, xz and yz planes through the centre of

the imaging volume are shown from top to bottom for each reconstruction. All reconstruction cases were scaled identically.

3.4 Discussion

3.4.1 Transducer and matching layer characterization

The transducers used in this work were built in-house, and there is inherently some variability in both their physical and signal detection properties. Applying matching layers by hand also contributed to variability in shape as well as transducer signal response. The variability between transducers was accounted for by using the same transducers for all matching layer cases. By characterizing the signal response of the same transducer both with and without shaped matching layers, changes were directly attributed to only the matching layer. Using the same four transducers for each matching layer case eliminated inter-transducer sensitivity variability as a concern as any differences contributed equally to each case. However, the physical variations between the transducers were not as well accounted for. The flat epoxy matching layer was applied to be flush with the transducer casing, but the depth of the face compared to the casing varied between transducers. Therefore, the shape and also the relative thickness of the matching layer contributed to the signal detection of the transducer. This concept is also true for the height of the convex epoxy matching layer. In this work, there was a maximum variability of 0.01 mm for flat epoxy application depth, and 0.41 mm for the height of the convex layer. Because there were not significant differences in the response between transducers for each matching layer case, it was determined that the height differences were acceptable for characterization. The thickness of the matching layer can also be optimized to broaden the bandwidth of the transducer in future work [17].

The application of a convex epoxy matching layer increased the absolute angular acceptance of the transducers only slightly. However, it did significantly decrease the signal from directly in front of the transducer face. In this way, the full width half maximum (FWHM) of the convex matching layer case was more than doubled compared to the flat matching layer case. The benefits of a large FWHM are that the sensitivity of the transducer is more uniform across a volume and thus contributes to an overall more uniform sensitivity for a transducer array. If the transducers are intended to detect weak

signal that are already barely distinguishable, such as those from deep within tissue, it would not be recommended to utilize a convex epoxy matching layer. However, when utilizing highly sensitive transducers such as those in this work and in other applications where there are strong PA signals, there is no concern of eliminating low pressure signals with the matching layer.

This work did not measure the acoustic properties of epoxy, although the material has been used successfully as a matching layer in the past [18]. In addition, only an epoxy-based matching layer was explored, although acrylic, PMMA, liquid sources, and a resin-based material have successfully been used to increase the angular acceptance of transducers elsewhere [12][19][20].

In implementation, it is not advisable to use transducers without a matching layer. Not only does the matching layer facilitate transfer of acoustic waves between the medium and transducer, but it also acts as protection from damaging highly sensitive detectors within the transducer. While the case with no matching layer was investigated in this work, it was primarily used to assess the effect of adding a matching layer on signal detection.

3.4.2 Simulated photoacoustic imaging system

A simulated photoacoustic imaging system was successfully used to predict the effects of matching layer shape on PA imaging outcomes. The sensitivity maps showed a large increase in uniformity throughout the imaging volume with a convex epoxy matching layer applied, but the absolute value of the sensitivity was up to 20 times lower than the alternative cases with no matching layer or a flat epoxy matching layer. This result was expected as the maximum signal amplitude detected by a transducer with a convex epoxy matching layer was nearly five times lower than that for the transducer case with no matching layer.

The MAE and SSIM index take both the sensitivity and aliasing of the system into account and offer a quantitative measure to assess matching layer cases. Both signal fidelity measures indicated that the no matching layer case performed optimally for all but the innermost region of the imaging volume, where the flat epoxy matching layer had

the lowest MAE and highest SSIM index. However, in the imaging task with a cubic array of points and Shepp-Logan phantom, the convex epoxy matching layer case had the most desirable signal fidelity measures in all cases but the SSIM index for the array of points, where all cases had the same result. The discrepancy between signal fidelity measures for analysis of the crosstalk matrix and of the imaging task was likely a result of the decreased signal amplitude for the convex matching layer case. Because each case was normalized independently, the ratio of signal to aliasing in the convex matching layer case was lower, though the absolute value of the aliasing was not significantly higher. The favourable results from the imaging task indicate that high signal is not necessary to accurately reconstruct targets. The MAE and SSIM index measures can be attributed to the more uniformly distributed sensitivity throughout the imaging volume. When translating these simulated results to a physical system, it would be beneficial to include convex epoxy matching layers to the transducer faces to optimize image reconstruction and verify the simulated results.

3.5 Conclusion

A 129 channel staring photoacoustic transducer array was successfully modeled to investigate the effects of a shaped epoxy matching layer on image reconstruction. Transducers with no matching layer displayed the highest signal detection sensitivity, transducers with a flat epoxy matching layer had a narrower angular acceptance than without a matching layer, and a convex epoxy matching layer reduced signal detection sensitivity and greatly increased the FWHM of the transducer detection. Analysis of the crosstalk matrix of each simulated case indicated that a convex matching layer would underperform compared to other matching layer cases, but in a simulated image reconstruction test it was shown to give optimal signal fidelity results. If PA signals are strong enough to be detected through a thick matching layer, increasing the FWHM of the transducer by applying a convex epoxy matching layer is capable of improving image reconstructions.

3.6 References

- [1] P. Beard, "Biomedical photoacoustic imaging.," *Interface Focus*, vol. 1, no. 4, pp. 602–31, Aug. 2011.
- [2] M. Xu and L. V. Wang, "Photoacoustic imaging in biomedicine," *Rev. Sci. Instrum.*, vol. 77, no. 4, p. 041101, 2006.
- [3] J. Xia, M. R. Chatni, K. Maslov, Z. Guo, K. Wang, M. Anastasio, and L. V Wang, "Whole-body ring-shaped confocal photoacoustic computed tomography of small animals in vivo.," *J. Biomed. Opt.*, vol. 17, no. 5, p. 050506, May 2012.
- [4] R. Ma, M. Distel, X. L. Deán-Ben, V. Ntziachristos, and D. Razansky, "Non-invasive whole-body imaging of adult zebrafish with optoacoustic tomography.," *Phys. Med. Biol.*, vol. 57, no. 22, pp. 7227–37, Nov. 2012.
- [5] M. P. Fronheiser, S. a Ermilov, H.-P. Brecht, A. Conjusteau, R. Su, K. Mehta, and A. a Oraevsky, "Real-time optoacoustic monitoring and three-dimensional mapping of a human arm vasculature.," *J. Biomed. Opt.*, vol. 15, no. 2, p. 021305, 2014.
- [6] R. A. Kruger, C. M. Kuzmiak, R. B. Lam, D. R. Reinecke, S. P. Del Rio, and D. Steed, "Dedicated 3D photoacoustic breast imaging.," *Med. Phys.*, vol. 40, no. 11, p. 113301, Nov. 2013.
- [7] K. S. Valluru, B. K. Chinni, N. A. Rao, S. Bhatt, and V. S. Dogra, "Development of a c-scan photoacoustic imaging probe for prostate cancer detection," vol. 7968, p. 79680C–79680C–7, Mar. 2011.
- [8] J. Gamelin, A. Aguirre, A. Maurudis, F. Huang, D. Castillo, L. V Wang, and Q. Zhu, "Curved array photoacoustic tomographic system for small animal imaging.," *J. Biomed. Opt.*, vol. 13, no. 2, p. 024007, 2013.
- [9] L. V Wang, "Multiscale photoacoustic microscopy and computed tomography.," *Nat. Photonics*, vol. 3, no. 9, pp. 503–509, Aug. 2009.
- [10] R. Bitton, R. Zemp, J. Yen, L. H. Wang, and K. K. Shung, "Design of a high frequency array based photoacoustic microscopy system for micro-vascular imaging.," *Conf. Proc. IEEE Eng. Med. Biol. Soc.*, vol. 2007, pp. 2175–8, Jan. 2007.
- [11] M. Xu and L. Wang, "Analytic explanation of spatial resolution related to bandwidth and detector aperture size in thermoacoustic or photoacoustic reconstruction," *Phys. Rev. E*, vol. 67, no. 5, p. 056605, May 2003.

- [12] M. Pramanik, G. Ku, and L. V Wang, "Tangential resolution improvement in thermoacoustic and photoacoustic tomography using a negative acoustic lens.," *J. Biomed. Opt.*, vol. 14, no. 2, p. 024028, 2014.
- [13] C. Song, L. Xi, and H. Jiang, "Acoustic lens with variable focal length for photoacoustic microscopy," *J. Appl. Phys.*, vol. 114, no. 19, p. 194703, 2013.
- [14] W. Xia, D. Piras, M. Heijblom, J. C. G. Van Hespén, S. Van Veldhoven, C. Prins, W. Steenbergen, T. G. Van Leeuwen, and S. Manohar, "Enlarged acceptance angle of a finite size detector in photoacoustic imaging using acoustic lenses," *Proc. SPIE-OSA*, vol. 8090, p. 80900L–80900L–7, Jun. 2011.
- [15] W. Xia, D. Piras, J. C. G. van Hespén, W. Steenbergen, and S. Manohar, "A new acoustic lens material for large area detectors in photoacoustic breast tomography," *Photoacoustics*, vol. 1, no. 2, pp. 9–18, May 2013.
- [16] M. Roumeliotis, R. Z. Stodilka, M. a Anastasio, G. Chaudhary, H. Al-Abed, E. Ng, A. Immucci, and J. J. L. Carson, "Analysis of a photoacoustic imaging system by the crosstalk matrix and singular value decomposition.," *Opt. Express*, vol. 18, no. 11, pp. 11406–17, May 2010.
- [17] W. Xia, D. Piras, M. Heijblom, J. Van Hespén, S. van Veldhoven, C. Prins, T. G. van Leeuwen, W. Steenbergen, and S. Manohar, "A custom-made linear array transducer for photoacoustic breast imaging," *Proc. SPIE*, vol. 8223, p. 82233D–82233D–6, Feb. 2012.
- [18] I. Kosik and J. J. L. Carson, "Real-time multispectral 3-D photoacoustic imaging of blood phantoms," *Proc. SPIE*, vol. 8581, p. 85811V, Mar. 2013.
- [19] W. Xia, D. Piras, J. C. G. van Hespén, W. Steenbergen, and S. Manohar, "A new acoustic lens material for large area detectors in photoacoustic breast tomography," *Photoacoustics*, vol. 1, no. 2, pp. 9–18, May 2013.
- [20] C. Song, L. Xi, and H. Jiang, "Liquid acoustic lens for photoacoustic tomography.," *Opt. Lett.*, vol. 38, no. 15, pp. 2930–3, Aug. 2013.

Chapter 4

4 Discussion and Future Work

This work focused on increasing the field of view of a photoacoustic staring transducer array. The directionality of transducers was investigated and it was determined that varying transducer direction may offer advantages for cubic targets of interest but is likely detrimental for imaging spherical or near-spherical specimens. A shaped matching layer was examined to increase the effective angular acceptance of transducers within the array, and the full width half maximum of the angular acceptance was largest for a convex epoxy matching layer. This chapter will discuss these results, limitation and caveats of the work, and future directions.

4.1 System characterization

4.1.1 Photoacoustic point source

In Chapter 2, the photoacoustic point source was characterized in order to make appropriate corrections to the signal received from transducers and model the system accordingly. While characterization of the point source was taken into consideration in this case, it is often assumed to be omnidirectional for the purpose of capturing the imaging operator for image reconstruction and system assessment. In Chapter 2 it was shown this was not the case, especially for high elevation angles. After the completion of the work in Chapter 2, another point source was fabricated using a 100 μm optical fiber and the same black connector coating described in 2.2.2. The fabrication procedure was identical for the two sources with only differing optical fiber diameters, yet the emission profile for the second point source was greatly varied from the first (Figure 4.1).

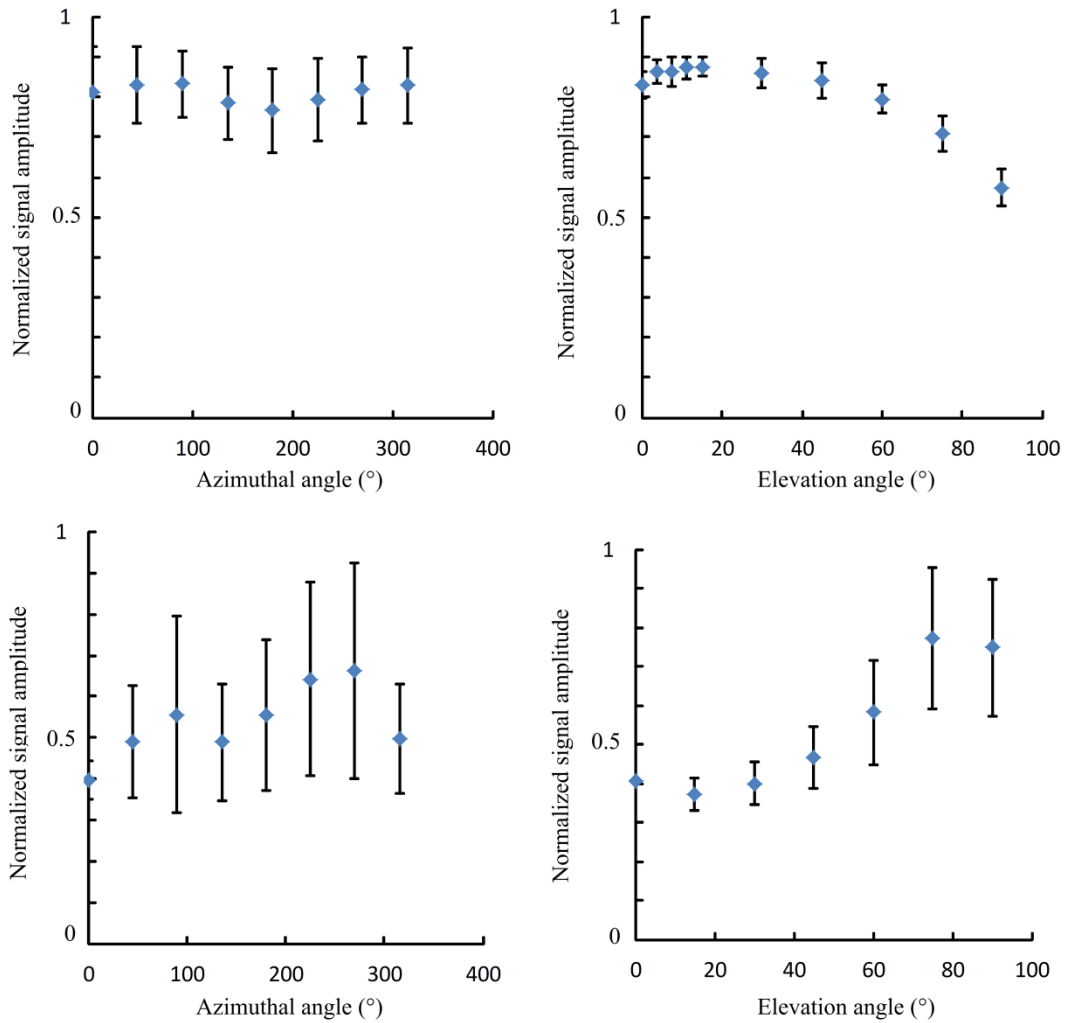


Figure 4.1: Emission profile of two point sources as a function of the azimuthal and elevation angles.

This discrepancy is most likely due to the manufacturing process of the point source, which was performed by hand. The polishing and coating of the optical fiber was performed as consistently as possible but the shape of both the fiber terminus and the black coating could not be strictly controlled and reproducibility is limited.

A completely omnidirectional point source is ideal for PAI system characterization so assumptions or corrections need not be made. Our group has previously developed an alternative PA point source utilizing methylene blue, intralipid and an optical fiber [1]. However, this approach caused staining of the optical fiber by the dye, resulting in decreased signal amplitude over time. Additional approaches include using a small absorber such as a spherical graphite particle or generating a photoacoustic

point source by rapid heating at the focal point of a laser beam [2][3]. Alternatively, the same variety of point source as used in this thesis could be illuminated externally rather than internally through the fiber. This may aid in uniform signal emission as the light is incident from a large solid angle surrounding the absorber. The external illumination method would also consider the light fluence of the system and this information then included in the imaging operator for reconstruction purposes.

4.1.2 Transducer characterization

The transducer characterization performed in Chapter 2 required correction for both point source irregularity and the distance between the transducer and point source. If an omnidirectional point source can be achieved, the characterization can be further improved by removing the second correction step. A new methodology was implemented in Chapter 3 to determine the angular acceptance of transducers that scans the point source in a semi-circular path about the transducer. This method maintained a fixed distance between the transducer and point source at all times and thus removed the distance correction.

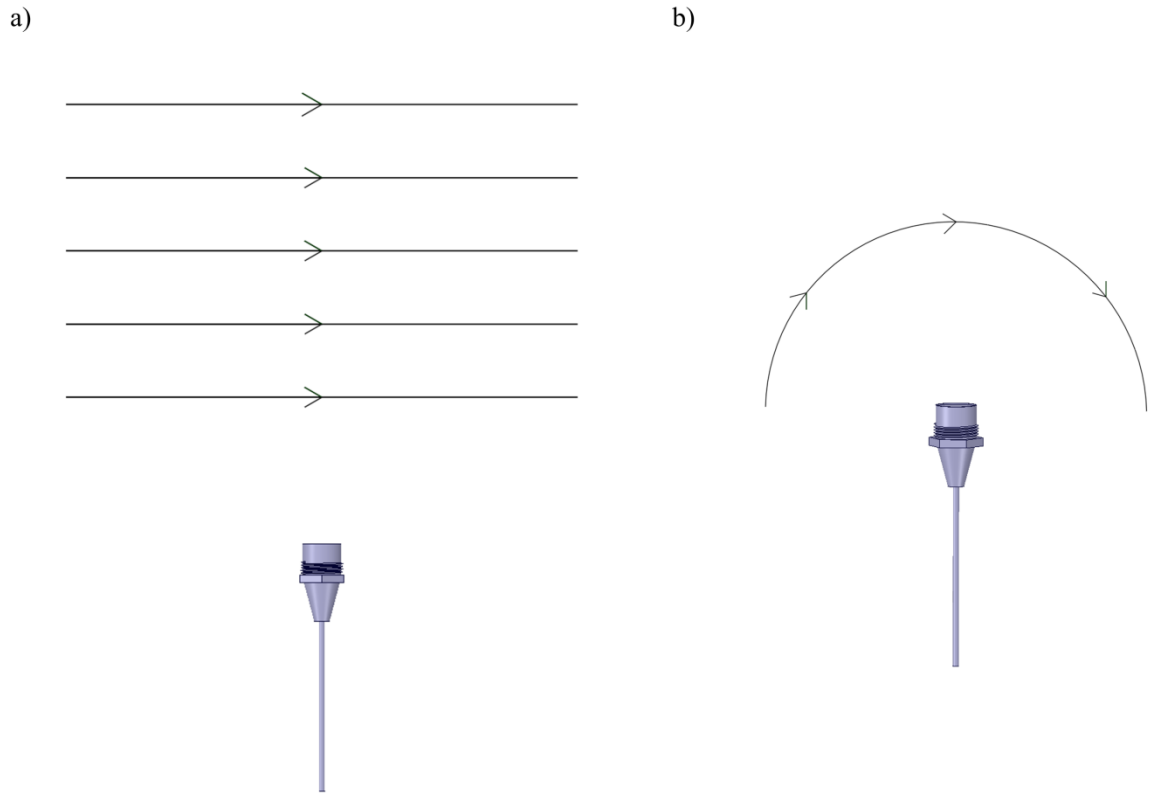


Figure 4.2: Visual depiction of two methods to determine the angular acceptance of a transducer implemented in this work. The point source was moved along the solid line in the direction shown by the arrow. (a) Raster scanning methodology used in Chapter 2 which required distance correction while (b) was implemented in Chapter 3 and maintained a fixed distance between the transducer and point source at all times. Images are not to scale.

In the simulated array in Chapter 2 it was assumed that all transducers in the array would behave similarly to the one characterized. However, due to manufacturing techniques and the transducers being built in-house, there is some variability between transducer signal responses. For this reason, several more transducers were characterized in the same manner as described in Chapter 2 to ensure that the representative transducer used as the basis of the array was not an outlier. It was found that the initial transducer was indeed representative of others in the array. An example of the angular acceptance of another transducer in the array is shown in Figure 4.3.

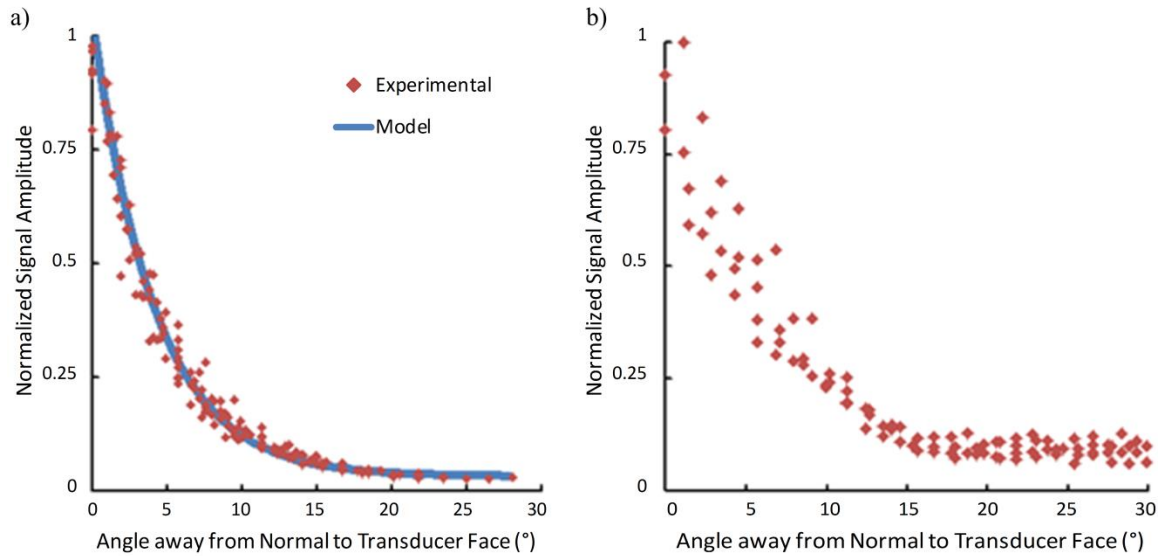


Figure 4.3: Transducer angular acceptance. (a) Figure 2.1 (d) shown again for comparison purposes where the red diamonds show experimental data and the blue line shows the mathematical model used in the simulated model of the system. (b) Example of the angular acceptance of another transducer from the PA array where red diamonds indicate experimentally collected data points from planes between 4 and 5 cm away from the transducer face.

A similar issue of variability between transducers was present in Chapter 3, using a hemispherical matching layer as an acoustic lens. The inherent variability of sensitivity and angular acceptance between transducers could not be avoided as the transducers had already been manufactured. In order to minimize the effect of inter-transducer variability, the same transducers were used to measure the response of each of the three matching layer cases. By averaging between the same four transducers, any differences in inherent sensitivity will be consistent throughout the matching layer cases. Thus, effects on sensitivity can be attributed to the shaped matching layer and not intrinsic variability between transducers. In addition, the epoxy used as a matching layer on each transducer face was applied by hand, and best judgment was used in order to assess the amount and final shape the epoxy would take. For flat matching layers, epoxy was applied to be flush with the transducer casing. A visual representation can be seen in Figure 4.4 (b). However, the depression between the transducer face and the case (Figure 4.4 (a)) is variable due to the manufacturing process. The results of Chapter 3 indicate that the more epoxy that is applied to the transducer face, the less signal sensitivity is maintained,

especially in the forward-facing direction. Minimizing the depth of the depression would be ideal in order to necessitate a smaller volume of epoxy and preserve signal sensitivity.

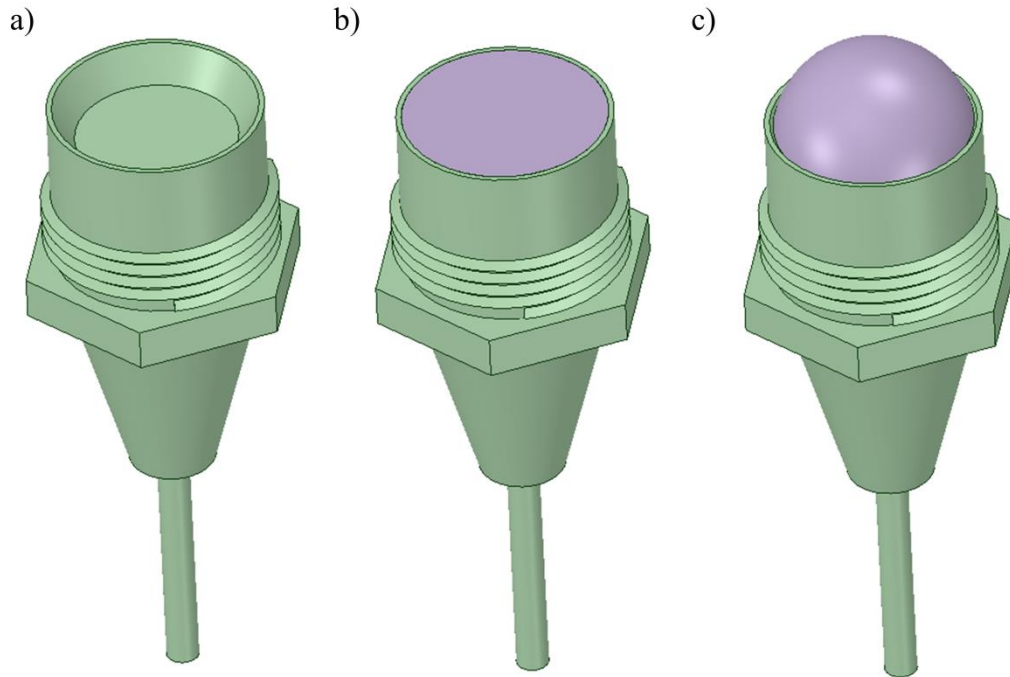


Figure 4.4: Three transducers with (a) no matching layer, (b) a flat epoxy matching layer, and (c) a convex epoxy matching layer, where epoxy is depicted in purple.

Only an epoxy matching layer was characterized as an acoustic lens in this work. As discussed in Chapter 1, acoustic lenses are not novel and acrylic lenses have been developed previously [4]. Epoxy was targeted as it had been used successfully as a matching layer in the past [5]. Epoxy also offered advantages for shaped layers as it is initially liquid, adherent to the transducer face, and hardens to a durable solid. Another resin-based material which is initially in a liquid state has been investigated and recommended for use as an acoustic lens, although lenses constructed from other materials should also be explored in order to augment existing transducers to the fullest [6].

4.1.3 System characterization

The imaging operators used for reconstruction in Chapter 2 and Chapter 3 were sparsely sampled with 1 mm voxels due to computational constraints, yet no research has

been conducted on the optimal voxel size in IO acquisition. It can be assumed that there is a lower limit at which image quality will no longer improve as voxel size decreases, and that this limit will be related to the number and spatial resolution of the transducers used in the system. However, more research is needed to determine the optimal balance between the step size used in the IO and the image quality.

In all previous work from our group, including both simulated and experimental work in this thesis, the imaging operator has been cubic in shape [5][7][8][9][10]. This was a result of the robotic system used to scan the point source throughout the imaging volume and the inherent Cartesian coordinates associated with it. However, most targets in PAI and biomedical imaging in general tend to be spherical or cylindrical in nature; whole-body small animal imaging can be generalized as a cylindrical and breast imaging and tumour specimens can be considered spherical, as examples. As such, the corners of the cubic imaging volume are seldom used. In future work cylindrical and/or spherical imaging operators should be explored to determine the effects on image quality as well as IO acquisition time and the computational load of calculating the pseudoinverse of the system.

4.2 Increasing the field of view of a photoacoustic transducer array

The directionality of transducers was explored in Chapter 2 and it was determined that all transducers oriented towards the centre of the array was optimal for spherical objects. As spherical or elliptical shaped surgical lumpectomy specimens motivated the imaging system, the directionality of the transducers remained toward the centre of the array. In Chapter 3, the FWHM of the signal sensitivity distribution was increased for transducers with a convex epoxy matching layer. A promising technique to increase the sampling and field of view of the array not covered in this work involves the use of acoustic reflectors within the transducer array. The concept of utilizing an acoustic reflector is that two (or more) distinct signals from different angles can be captured by each detector with a single laser shot (Figure 4.5). To increase the FOV, reflectors can be oriented such that the signal being directed at transducers is from regions outside of their FOV. Several groups have proposed and implemented acoustic reflectors using single transducers and linear arrays as a proof of concept [11][12][13].

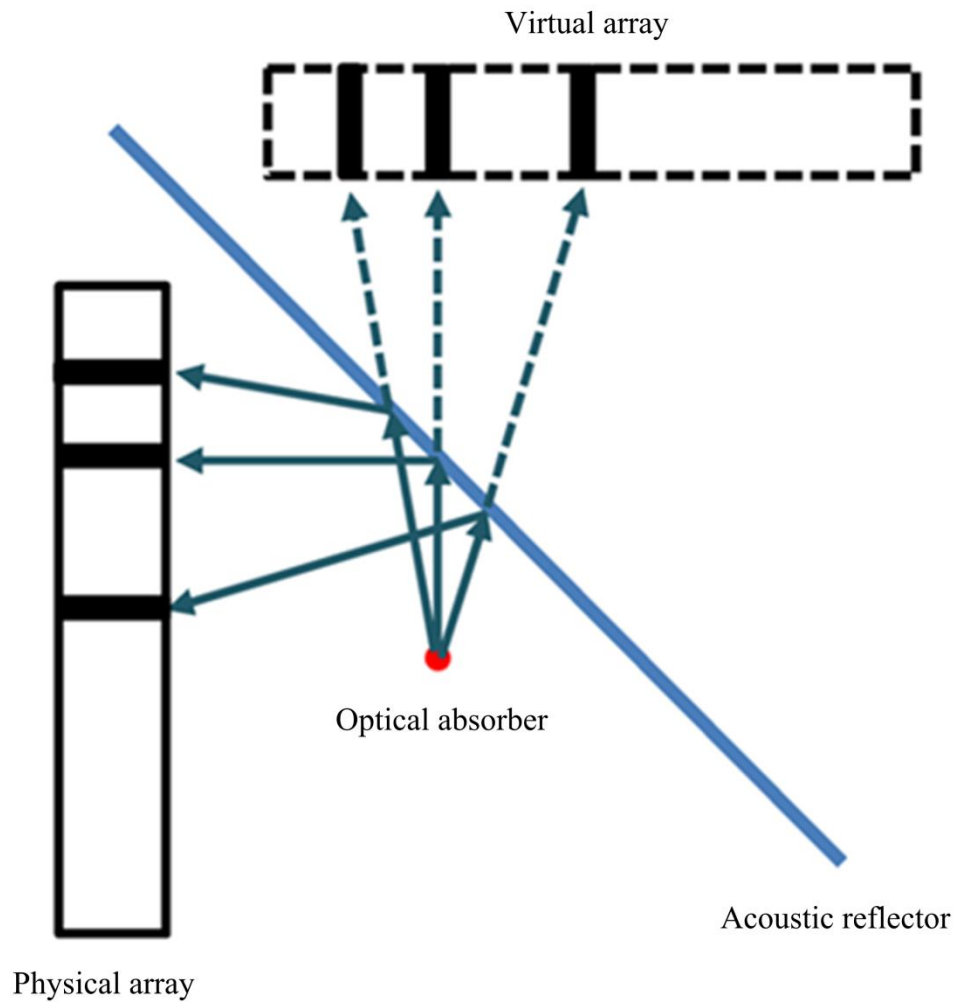


Figure 4.5: A photoacoustic imaging system design utilizing an acoustic reflector. Adapted from Huang et al. [13].

4.3 Image reconstruction

Model-based reconstruction has advantages over theoretical reconstruction techniques as it can account for all aspects of the imaging system, which may or may not be included in a theoretical approach. When inverting an experimental imaging operator by SVD many of the singular values are disposed of by regularization. The amount of regularization performed is currently an empirical process. Studying the effects of

regularization on the imaging outcomes of the system would allow for more robust selection criteria and provide a standard across imaging platforms.

4.4 System analysis

In Chapters 2 and 3 the crosstalk matrix sensitivity and aliasing along with the mean absolute error and structural similarity index were used to assess system performance. While these signal fidelity measures were an improvement over the crosstalk matrix alone, additional measures exist to assess signal and system performance. For biomedical applications, the sensitivity and specificity of a system for a specific application (e.g. cancer detection) would serve to be the ultimate assessment of the system's performance and should be compared against the current gold standard for that application (e.g. histopathology).

4.5 Applications

The biomedical applications of this system can be extended from *ex vivo* human sample imaging to *in vivo* mouse imaging. The high temporal resolution of the system makes it uniquely capable of performing high-speed anatomical and functional imaging *in vivo* using either endogenous or exogenous contrast. Mouse and rat brain function can be measured by mapping blood saturation in real-time and small animal tumour models can be monitored non-invasively with endogenous contrast in a non-destructive manner.

4.5.1 A photoacoustic imaging system for lumpectomy margin assessment

The most immediate future work to be carried out will involve imaging of surgical lumpectomy specimens. To acquire preliminary data for the translation of FOV increasing techniques into an experimental system, 128 transducers were surfaced with a convex epoxy matching layer and installed in a physical array equivalent to that modeled and shown in Figures 2.2 (c) and 3.3 (a). To begin characterization of the system, an imaging operator scan of one xy plane in the centre of the imaging volume was captured. In order to capture the imaging operator, a point source mounted on a SCARA robot (Model E2C351A – UL, Epson) was scanned through a 2.1 x 2.1 cm imaging volume with 1 mm step size, corresponding to 21 x 21 grid locations. Unlike previous imaging operators captured with our system, the point source was illuminated from four fiber

bundles located in the top rung of the transducer array. The PA signal generated by the point source at each grid location was recorded for all transducers. The crosstalk matrix was calculated from the imaging operator to find the sensitivity of the array and is shown in Figure 4.6.

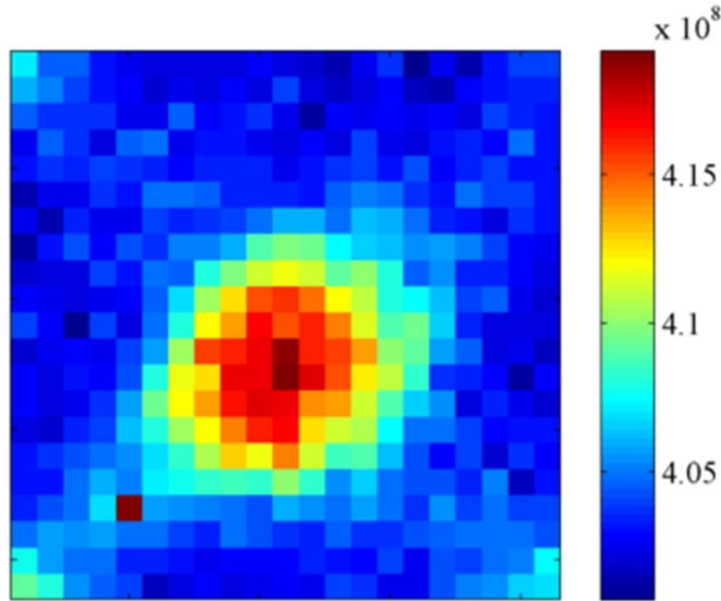


Figure 4.6: Sensitivity map of the centre z plane of the imaging volume, where each side is 2.1 cm and the colour represents sensitivity to signals in that voxel.

The sensitivity map has not been corrected for laser output and the dark red voxel in the lower left quadrant is likely due to higher output from the laser for one shot in the scan. Three corners of the plane appear to have higher sensitivity than other regions in the periphery of the plane. This is due to the uncorrected imaging operator which, because the point source was illuminated externally, accounts for fluence in the imaging volume. The four fiber bundles were located near each corner of the plane and thus the light fluence is higher in these regions.

When considering the absolute value of the sensitivity of the plane, it was quite uniform throughout; there was a variation of approximately 5% from the lowest to highest values. In this case, the FWHM is beyond the limits of the plane. If the values within the plane are normalized between 0 and 1, the FWHM is found to be approximately 1 cm. This FWHM is comparable with our previous system, however, final conclusions cannot be made until imaging results are compared. The low variability

in sensitivity for the absolute values indicates the system may be able to detect more uniformly across the volume than the previous PAI system, allowing for the accommodation of lumpectomy specimens.

4.6 Summary and conclusions

It was proposed by the work in this thesis that the field of view of a photoacoustic transducer array could be increased without replacing the detectors in the array. In Chapter 2, the effect of the directivity of transducers within an imaging array on the FOV was explored by simulating an existing PAI system. It was found that although varying the directionality of transducer may offer improvements for cubic imaging volumes, it is detrimental to imaging spherical specimens in the array. In Chapter 3, a matching layer was used as an acoustic lens to increase the angular acceptance of transducers. The full width half maximum of transducer angular acceptance using a convex epoxy matching layer was increased by more than two times the FWHM of transducers with no or flat matching layers. The nearly uniform sensitivity of the centre plane of a staring transducer array populated with transducers with convex epoxy matching layers was shown in Chapter 4, although imaging results are needed to confirm system improvements. The addition of a shaped matching layer can be applied to many transducers and this technique could improve the FOV of transducer arrays across the field of PAI. The improved FOV of our system will allow for lumpectomy specimen imaging and permit an assortment of anatomical and functional biomedical imaging in the future.

4.7 References

- [1] M. Roumeliotis, P. Ephrat, J. Patrick, and J. J. L. Carson, “Development and characterization of an omni-directional photoacoustic point source for calibration of a staring 3D photoacoustic imaging system,” *Opt. Express*, vol. 17, no. 17, p. 15228, Aug. 2009.
- [2] B. Wang, L. Xiang, M. S. Jiang, J. Yang, Q. Zhang, P. R. Carney, and H. Jiang, “Photoacoustic tomography system for noninvasive real-time three-dimensional imaging of epilepsy,” *Biomed. Opt. Express*, vol. 3, no. 6, pp. 1427–32, Jun. 2012.
- [3] J. G. Bolaños, V. Pulkki, P. Karppinen, and E. Hæggström, “An optoacoustic point source for acoustic scale model measurements,” *J. Acoust. Soc. Am.*, vol. 133, no. 4, pp. EL221–7, Apr. 2013.
- [4] W. Xia, D. Piras, M. Heijblom, J. C. G. Van Hespén, S. Van Veldhoven, C. Prins, W. Steenbergen, T. G. Van Leeuwen, and S. Manohar, “Enlarged acceptance angle of a finite size detector in photoacoustic imaging using acoustic lenses,” *Proc. SPIE-OSA*, vol. 8090, pp. 80900L–1–7, Jun. 2011.
- [5] I. Kosik and J. J. L. Carson, “Real-time multispectral 3-D photoacoustic imaging of blood phantoms,” *Proc. SPIE*, vol. 8581, p. 85811V, Mar. 2013.
- [6] W. Xia, D. Piras, J. C. G. van Hespén, W. Steenbergen, and S. Manohar, “A new acoustic lens material for large area detectors in photoacoustic breast tomography,” *Photoacoustics*, vol. 1, no. 2, pp. 9–18, May 2013.
- [7] M. Roumeliotis, R. Z. Stodilka, M. a Anastasio, G. Chaudhary, H. Al-Abed, E. Ng, A. Immucci, and J. J. L. Carson, “Analysis of a photoacoustic imaging system by the crosstalk matrix and singular value decomposition,” *Opt. Express*, vol. 18, no. 11, pp. 11406–17, May 2010.
- [8] P. Wong, I. Kosik, and J. J. L. Carson, “Dynamic contrast-enhanced 3D photoacoustic imaging,” *Proc. SPIE*, vol. 8581, p. 858152, Mar. 2013.
- [9] P. Tavakolian, I. Kosik, A. Chamson-Reig, K. St. Lawrence, J. J. L. Carson, R. Todd, and F. Vasefi, “Potential for photoacoustic imaging of the neonatal brain,” *Proc. SPIE*, vol. 8581, p. 858146, Mar. 2013.
- [10] J. J. L. Carson, P. Ephrat, and A. Seabrook, “Measurement of photoacoustic transducer position by robotic source placement and nonlinear parameter estimation,” *Proc. SPIE*, vol. 6856, no. 1, p. 68561Z–68561Z–8, 2008.

- [11] D. Tsyboulski, A. Conjusteau, S. a. Ermilov, H.-P. F. Brecht, A. Liopo, R. Su, V. Nadvoretzky, and A. a. Oraevsky, "Optoacoustic imaging system with improved collection efficiency.," *Proc. SPIE*, vol. 7899, p. 78991D–78991D–8, Feb. 2011.
- [12] L. Kunyansky, B. Holman, and B. T. Cox, "Photoacoustic tomography in a rectangular reflecting cavity," *Inverse Probl.*, vol. 29, no. 12, p. 125010, Dec. 2013.
- [13] B. Huang, J. Xia, K. Maslov, and L. V Wang, "Improving limited-view photoacoustic tomography with an acoustic reflector.," *J. Biomed. Opt.*, vol. 18, no. 11, p. 110505, Jan. 2013.
- [14] L. Xi, S. R. Grobmyer, L. Wu, R. Chen, G. Zhou, L. G. Gutwein, J. Sun, W. Liao, Q. Zhou, H. Xie, and H. Jiang, "Evaluation of breast tumor margins in vivo with intraoperative photoacoustic imaging.," *Opt. Express*, vol. 20, no. 8, pp. 8726–31, Apr. 2012.

Curriculum Vitae

Name	Avery Raess
Post-secondary Education and Degrees	M.Sc., Medical Biophysics, University of Western Ontario. (2012 – 2014) B.Sc., Medical Physics, Ryerson University. (2008 – 2012)
Academic Awards and Achievements	Canadian Institutes of Health Research Frederick Banting and Charles Best Canada Graduate Scholarship, 2013 – 2014. Canadian Institutes of Health Research Strategic Training Program in Cancer Research and Technology Transfer, 2013 – 2014. Translational Breast Cancer Studentship from the London Regional Cancer Program, 2013 – 2014. Ontario Graduate Scholarship, 2012 – 2014. (declined in 2013 – 2014) Western Graduate Research Scholarship, 2012 – 2014. Natural Sciences and Engineering Research Council of Canada Undergraduate Student Research Award, 2010 – 2012. Dean's Honour List, Ryerson University, 2008 – 2012. Ryerson University Entrance Scholarship, 2008 – 2012. Second place poster presentation at Engineering Medical Innovation, Toronto, 2012. Physics Undergraduate Alumni Award for excellence in the second year of the Medical Physics program, Ryerson University, 2010. Clyde Logue Award for excellence in first year Physics, Ryerson University, 2009.
Presentations	Raess A, Wong P, Kosik I, Carson JLL. Investigation of a photoacoustic imaging system with multiple focal points. Poster presentation at the 11 th Annual Oncology Research and Education Day (2014). London, ON. Raess A, Wong P, Kosik I, Carson JLL. Investigation of a photoacoustic imaging system with multiple focal points. Poster presentation at London Health Research Day (2014). London, ON. Raess A, Wong P, Kosik I, Carson JLL. Investigation of a photoacoustic imaging system with multiple focal points. Poster

presentation at the 12th Imaging Network Ontario Symposium (2014). Toronto, ON.

Raess A, Wong P, Kosik I, Carson JLL. Investigation of a photoacoustic imaging system with multiple focal points. Poster presentation at the 2014 London Health Research Day. London, ON.

Raess A, Wong P, Kosik I, Carson JLL. Model based optimization of a staring transducer array for photoacoustic imaging. Poster presentation at the 10th Annual Oncology Research and Education Day (2013). London, ON.

Raess A, Wong P, Kosik I, Carson JLL. Characterization of a photoacoustic imaging array. Oral Presentation at the 2013 Artimino Ultrasound Conference. Lake Rosseau, ON.

Raess A, Wong P, Kosik I, Carson JLL. Model based optimization of a staring transducer array for photoacoustic imaging. Poster presentation at the 2013 London Health Research Day. London, ON.

Raess A, Ailenberg M, Rostein O, Karshafian R. Enhancing gene transfection in vitro using ultrasound and microbubbles. Second place poster presentation at the 2012 Engineering Medical Innovation Symposium. Toronto, ON.

Raess A, Ailenberg M, Rostein O, Karshafian R. Enhancing gene transfection in vitro using ultrasound and microbubbles. First place at the 2012 Ryerson Thesis Poster Presentation Session. Toronto, ON.

Raess A, Ailenberg M, Rostein O, Karshafian R. Enhancing gene transfection in vitro using ultrasound and microbubbles. Poster presentation at the 2012 Chemical Biophysics Symposium. Toronto, ON.

Raess A, Kolios M. High-frequency ultrasound backscatter from single cells and microbubbles. Poster presentation at the 2011 Canadian Undergraduate Physics Conference. Saskatoon, SK.